

GNSS/Multi-Sensor Fusion Using Continuous-Time Factor Graph Optimization for Robust Localization

Haoming Zhang¹, *Member, IEEE*, Chih-Chun Chen¹,
Heike Vallery^{1,2}, *Member, IEEE* and Timothy D. Barfoot³, *Fellow, IEEE*

Abstract—Accurate and robust vehicle localization in highly urbanized areas is challenging. Sensors are often corrupted in those complicated and large-scale environments. This paper introduces GNSS-FGO, an online and global trajectory estimator that fuses GNSS observations alongside multiple sensor measurements for robust vehicle localization. In GNSS-FGO, we fuse asynchronous sensor measurements into the graph with a continuous-time trajectory representation using Gaussian process regression. This enables querying states at arbitrary timestamps so that sensor observations are fused without requiring strict state and measurement synchronization. Thus, the proposed method presents a generalized factor graph for multi-sensor fusion. To evaluate and study different GNSS fusion strategies, we fuse GNSS measurements in loose and tight coupling with a speed sensor, IMU, and lidar-odometry. We employed datasets from measurement campaigns in Aachen, Düsseldorf, and Cologne in experimental studies and presented comprehensive discussions on sensor observations, smoother types, and hyperparameter tuning. Our results show that the proposed approach enables robust trajectory estimation in dense urban areas, where the classic multi-sensor fusion method fails due to sensor degradation. In a test sequence containing a 17 km route through Aachen, the proposed method results in a mean 2D positioning error of 0.19 m for loosely coupled GNSS fusion and 0.48 m while fusing raw GNSS observations with lidar odometry in tight coupling.

Index Terms—GNSS, Factor Graph Optimization, Localization, Sensor Fusion, Autonomous Vehicle Navigation

I. INTRODUCTION

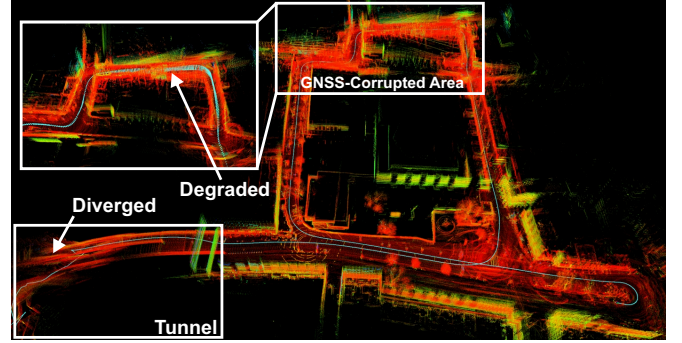
Safe and reliable autonomous driving operations in urban areas require accurate and consistent vehicle localization that infers a smooth trajectory estimate for planning and control tasks. Autonomous vehicles may use global navigation satellite systems (GNSS) to achieve global positioning in large-scale environments. However, the performance of GNSS is highly degraded when a vehicle passes through tunnels or urban canyons, where GNSS signal loss can be expected, greatly penalizing positioning availability. Moreover, the error dynamics of GNSS observations grow increasingly complex due to multipath and non-line-of-sight effects, resulting in inconsistent error models used in state estimation [1].

¹H. Zhang, C.-C. Chen, and H. Vallery are with the Institute of Automatic Control, Faculty of Mechanical Engineering, RWTH Aachen University, Aachen, Germany.

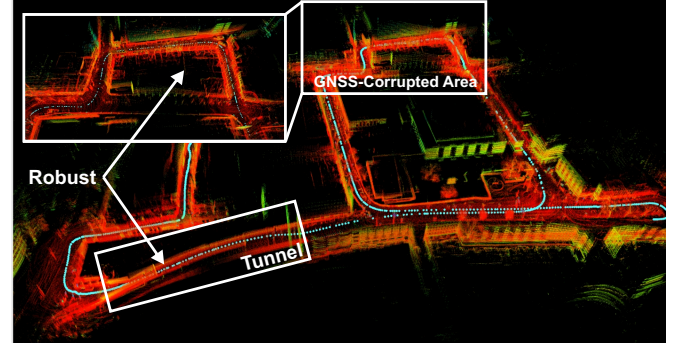
²H. Vallery is also with the Department of BioMechanical Engineering, Delft University of Technology, and with the Department for Rehabilitation Medicine, Erasmus MC, Rotterdam, The Netherlands.

³T. D. Barfoot is with the University of Toronto Robotics Institute, Toronto, Canada.

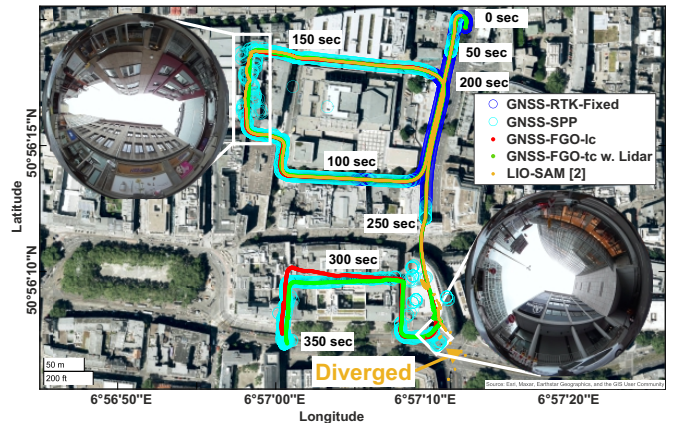
Corresponding author: h.zhang@irt.rwth-aachen.de



(a) Lidar map and trajectory using LIO-SAM [2]. This approach fused with GNSS positioning failed due to faulty scan registrations while crossing a tunnel and degrades dramatically with corrupted GNSS measurements.



(b) Lidar map and trajectory using GNSS-FGO (ours). The proposed method provides robust trajectory estimation and suffers from only slight degradation in GNSS-corrupted areas.



(c) Estimated trajectories. The fisheye images show challenging areas where the GNSS observations are blocked or strongly corrupted.

Figure 1: Demonstration of multi-sensor fusion for vehicle localization of test sequence C02 in the city of Cologne.

Many previous works fuse information from local optical sensors (e.g., lidars or cameras) for vehicle localization. They can typically be categorized into pose retrieval using a given map [3] and simultaneous location and mapping (SLAM) [4]. Generally, landmarks in sensor frames are extracted and associated to acquire either frame-to-map global pose constraints or frame-to-frame local motion increments. Lacking high-quality maps for vehicle pose retrieval in many areas, approaches relying on local sensors can often only achieve satisfactory localization if the ground is even and sufficient loop-closure constraints help eliminate drift. However, these requirements cannot always be met for long-term autonomous operations in large-scale environments [5].

In recent years, combining local sensors with GNSS has been investigated as a robust way to enable accurate and precise vehicle location in challenging areas. Incremental batch estimation implemented as factor graph optimization (FGO) is often superior to classic filtering-based algorithms in terms of localization performance and consistency [6, 7]. Unlike Bayesian filters, a factor graph fuses prior information and sensor measurements associated with the to-be-estimated state variables into probabilistic representations. A maximum-a-posterior problem (MAP) can be formulated from the factor graph and solved in a batch configuration using iterative Gauss-Newton-like algorithms [8]. In general, this optimization procedure is activated only if new sensor observations are available. Thus, many classic graph FGO approaches rely on a primary sensor that schedules the optimization procedure.

To fuse additional sensor modalities, asynchronous measurements must be synchronized with the primary sensor, leading to information loss and inefficient fusion mechanisms. Furthermore, classic FGO approaches degrade if the primary sensor is compromised or fails, which is likely in challenging environments. In this case, state variables cannot be effectively constrained by other sensor observations if the graph is not constructed in time. Fig. 1 exemplifies this problem, where a state-of-the-art lidar-centric SLAM approach diverges due to scan registration failures while driving in a tunnel¹. In fact, as discussed in [9]–[11], commonly used sensors in localization deteriorate under challenging environmental conditions, complicating robust and long-term vehicle localization.

In this work, we address the degradation problem of GNSS-based localization approaches by translating classic FGO for multi-sensor fusion into an approach where the graph associated with all to-be-estimated state variables is constructed deterministically based on a priori chosen timestamps. It thus presents a time-centric factor graph construction that is independent of any particular reference sensor (e.g., GNSS). To achieve this, we represent the vehicle trajectory in continuous time using a Gaussian process (GP). This approach incorporates a motion prior using the white-noise-on-jerk (WNOJ) motion model, as originally proposed in [12]. The algorithm feeds new observations from each sensor independently into the factor graph without measurement-to-state synchronization. If a measurement cannot be temporally aligned with any

state variable, we query a GP-interpolated state corresponding to the measurement that is used for the error evaluation within the optimization procedures.

To retrieve a robust global trajectory estimation while the GNSS measurements are strongly corrupted, we implemented the time-centric factor graph to fuse GNSS observations with measurements of an inertial measurement unit (IMU), optical speed sensor, and lidar for vehicle localization in challenging urban scenarios. We propose two factor graph structures for both loosely and tightly coupled fusion of GNSS observations alongside other local sensor measurements, demonstrating the flexibility of the proposed GNSS-FGO. For the graph that considers the GNSS positioning solution in the loose coupling, we fuse the pre-integrated IMU measurements, 2D velocity measurements, and lidar odometry. In tightly coupled fusion, we replace GNSS solution factors with GNSS pseudorange and deltarange factors, which are expected to provide more effective constraints compared to inconsistent GNSS positioning in urban areas [6].

We used raw data from measurement campaigns in the cities of Aachen, Düsseldorf, and Cologne to evaluate the proposed approach by benchmarking with a well-known lidar-centric SLAM approach [2, 13]. This lidar-centric SLAM has been shown to perform best for vehicle localization tasks in large-scale environments and can be configured to fuse GNSS measurements [14], which presents an equivalent fusion mechanism as our loosely coupled GNSS-FGO.

In contrast to our previous study [7], which focused only on trajectory smoothness using FGO with an offline evaluation, we now address online multi-sensor fusion for vehicle localization.

The contributions of this work are summarized as follows:

- 1) We propose a flexible, online, continuous-time factor graph optimization framework that can accommodate common multi-sensor fusion problems. The flexibility comes from the fact that (i) we can accommodate asynchronous measurements, and (ii) we choose estimation timestamps independent of any particular sensor frequency. This latter feature, as well as the smoothing effect of a motion prior, provide robustness in the phase of any particular sensor dropout.
- 2) We implement the proposed method for vehicle localization in challenging scenarios and conduct comprehensive studies on loosely coupled and tightly coupled fusion mechanisms to fuse GNSS measurements with other local sensors, with the aim of presenting extensive evaluations and discussions on accuracy, robustness, and run-time efficiency. Compared to other state-of-the-art methods, our method is shown to be more robust in our challenging test scenarios.
- 3) We evaluate the GP motion prior, which is implemented using the white-noise-on-acceleration (WNOA) and white-noise-on-jerk (WNOJ) models, to study the accuracy of the interpolated states.
- 4) We introduce a scalable and open-source software framework `gnssFGO2` that can be extended for arbitrary robot localization using continuous-time factor graph optimization.

¹Same factors, noise models, and smoother were used while benchmarking the lidar-centric approach with loosely coupled GNSS-FGO.

The rest of this article is organized as follows: we present a comprehensive review of the literature on multi-sensor fusion in the context of vehicle location using FGO in Sec. II. Sec. III introduces the proposed continuous-time FGO in detail. In Sec. IV, the mathematical background for factor formulations is presented, whereas the graph implementations for vehicle localization are introduced in Sec. V. We verify our method in Sec. VII and conduct further experiments and ablation studies on the precision and consistency of estimated trajectories in different scenarios. Finally, Sec. VIII summarizes results and limitations. We release our code and raw data used in our experiments from real-world measurement campaigns with different urban scenarios². A demonstration video is also available³.

II. RELATED WORK

A. Graph Optimization for GNSS-based Vehicle Localization

In recent years, fusing GNSS observations using factor graph optimization for robust vehicle localization has drawn great attention. Compared with filtering-based approaches, FGO conducts batch optimization, where all measurement models are re-linearized and re-evaluated iteratively, resulting in a more robust state estimation even with measurement outliers. Previous work demonstrated robust localization in urban areas only by factoring pseudoranges with robust error models [15, 16]. Later, Wen et al., [6] and Zhang et al., [7] showed that FGO generally outperforms Kalman filters with respect to the precision and smoothness of the estimated trajectory.

GNSS data can be integrated into the graph using a loosely or tightly coupled schema [17]. While the loosely coupled fusion incorporates GNSS positioning solution into the graph, pre-processed raw GNSS observations such as code or carrier phase measurements can be fed into the estimator in a tight coupling as state constraints. As the to-be-estimated state variables can be directly observed in GNSS solutions, fusing GNSS data in a loose coupling enables quick convergence and elevated accuracy if high-quality Real-Time-Kinematic (RTK)-fixed GNSS solutions are available. In contrast, the integration of raw GNSS observations contributes to multiple state constraints associated with received satellites, which has been shown to be more robust than loose coupling [6, 18, 19]. Wen et al. [20] included double-differenced pseudorange (DDPR) and double-differenced carrier-phase measurements (DDCP) in FGO, resulting in performance improvement. Later, this work was extended to efficiently model carrier-phase constraints between multiple satellite measurement epochs within a time window [21]. In [22], time-differenced carrier-phase (TDCP) was integrated with cycle-slip estimation, which achieved accurate localization while presenting substantial availability compared to DDCP if satellites can be continuously tracked. Congram and Barfoot [23] also proposed a GPS odometry using TDCP with a more prominent cycle-slip detection and showed an effective drift reduction compared to visual odometry. However, since carrier-phase observations

are also disturbed in deep urban areas, the robustness of state estimation cannot yet be guaranteed.

As factor graph optimization presents a convenient tool for robust error modeling [24], several works employ m-Estimators to reject faulty GNSS observations [7, 16, 22, 25, 26]. Recently, FGO has been explored in the context of vehicle location based on GNSS for noise distribution identification or adaptive rejection of outliers [27, 28], showing a positive impact on consistent trajectory estimation using FGO.

B. Graph Optimization for Multi-Sensor Fusion

While the aforementioned works have particularly explored graph optimization for GNSS observations, they may still suffer from performance degeneration in complex scenarios if GNSS measurements are lost or present outliers. Therefore, another research domain focuses on fusing more sensor modalities (more than two) alongside GNSS observations into the graph, with applications predominantly in SLAM.

A pose graph that fuses GPS position measurements and lidar odometry with loop-closure constraints for outdoor scenarios improved both runtime efficiency and performance compared to lidar-only approaches [29]. In [2], feature-based lidar odometry and loop-closure constraints were merged into a factor graph with synchronized GPS position measurements to achieve a drift-free pose estimate, which was forwarded to another graph optimization with pre-integrated IMU measurements for high-frequency and real-time state estimation. In addition to integrating feature-based lidar odometry into FGO, the lidar map can also be used for GNSS visibility assessment [30]. Some works also introduce camera-centric sensor fusion, where other sensor observations are synchronized with camera data and fused on the graph [31]–[33]. In [34], camera, lidar, and wheel odometers were fused into the graph along with the GNSS positioning solution and IMU measurements, presenting consistent localization in featureless environments for long-term runs. Similar works also conduct multi-sensor fusion without GNSS and propose a carefully managed fusion architecture [35, 36]. However, these works still require well-handled data synchronization and careful graph construction to fuse heterogeneous sensor measurements.

Many recent approaches introduce multi-graph structures to achieve flexible and compact sensor fusion. In [37], IMU, GNSS, and lidar observations were separately integrated into multiple graphs in parallel with a switching mechanism. When the GNSS receiver lost its signal, the lidar-centric graph was activated. Another work aimed to confederate loosely and tightly coupled fusion schemes to ensure the estimation performance [38]. Each sensor modality is associated with a separate graph and proposes odometry factors to the IMU-centric graph that provides final estimated states in real-time.

Because the aforementioned methods introduce redundant and complex graph structures, other works exploit high-frequency IMU measurements to coordinate multi-sensor fusion. In [39] and [40], asynchronous global pose measurements (e.g., GPS measurements) are propagated into timestamps of visual-inertial factors using pre-integrated IMU measurements. The same concept has been extended to a forward-backward

²<https://github.com/rwth-irt/gnssFGO>

³<https://youtu.be/9R55uCCrNss>

IMU pre-integration mechanism in order to precisely associate asynchronous measurements with keyframes [41]. Nevertheless, these methods still depend on the noisy IMU sensor, which introduces uncertainty.

C. Continuous-Time Trajectory Representation

One essential requirement for flexible graph-based multi-sensor fusion is the ability to query the states associated with the observations within the iterative optimization process. This requirement can be fulfilled if the trajectory is represented in continuous time. In [42], B-splines were proposed as a parametric approach to represent the trajectory in continuous time. This method was later used to propose stereo-inertial odometry [43]. Another approach utilizes exactly sparse Gaussian process (GP) regression by assuming that system dynamics follow a linear time-varying stochastic differential equation (LTV-SDE) [44]. The system dynamics are typically modeled as white-noise-on-acceleration (WNOA). This approach was verified in [45]–[47], where the reliability of this proposed surrogate dynamics model was demonstrated. Recently, Tang et al. [12] proposed an improved system dynamics model, which assumed a white-noise-on-jerk (WNOJ) model in LTV-SDE. They showed that the WNOJ could model the vehicle dynamics more accurately and thus, was appropriate for systems with more complicated dynamics. This work follows this aspect and adapts the GP-WNOJ model proposed in [12] as between-state motion constraints and state interpolator to fuse asynchronous measurements.

Although continuous-time trajectory representation is studied for localization and mapping problems by extending incremental smoothing using sparse GP interpolation to reduce computation time [46], fusing GNSS observations with multiple heterogeneous sensor measurements for online vehicle localization has not yet been presented or discussed. Inspired by the aforementioned methods, we address the problem of multi-sensor fusion for GNSS-based vehicle localization using continuous-time trajectory representation, which enables a fusion of asynchronous sensor observations in a single factor graph. Our hypotheses are: (i) factor graph construction in continuous time generalizes multi-sensor fusion and enables consistent trajectory estimation that incorporates effective state constraints from multiple sensor modalities in challenging scenarios, (ii) the GP-WNOJ motion model presents a larger capacity to represent complicated system dynamics, such as driving in urban areas.

III. TIME-CENTRIC FACTOR GRAPH OPTIMIZATION

In this section, we introduce an implementation of continuous-time trajectory estimation, as proposed in [12, 44]. Generally, fusing multiple heterogeneous sensor observations into a state estimator incorporates different timestamps due to asynchronous measurements and unpredictable delays. In this work, we assume that the state estimator and all measurements have the same timing clock. Compared to the estimated states in continuous time, all sensor observations are sampled and processed in asynchronous timestamps, as illustrated in Fig. 2. We employ GP motion priors that enable a continuous-time

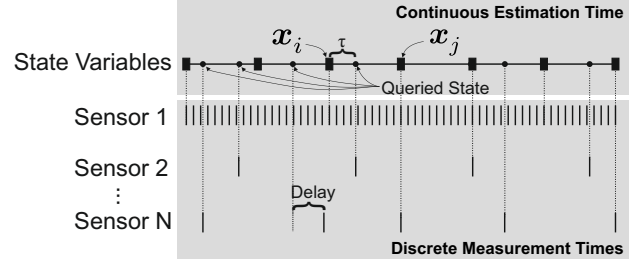


Figure 2: Continuous-time state estimation with asynchronous measurements. A time offset τ can be calculated with respect to a former state variable for each asynchronous measurement.

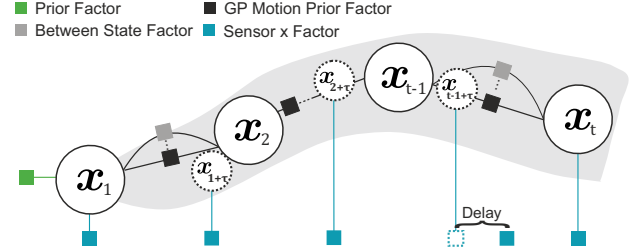


Figure 3: A general time-centric factor graph. The state variables x_t are created and constrained with GP motion prior factors on time while all asynchronous measurements are fused by querying a state with a time offset τ to a former state variable.

trajectory representation. In this way, the construction of a factor graph can be deterministic and time-centric, bypassing asynchronous sensor frequencies and timing issues. We show the general structure of a time-centric factor graph in Fig. 3, where the to-be-estimated state variables x_t are presented in solid line circles on a continuous-time trajectory. The queried states in dashed lines are not explicitly estimated in the optimization procedure, and thus are only queried between two successive state variables using the time offset τ to the previous state variable.

Alg. 1 explains one optimization procedure from graph construction to iterative optimization. Assume that the time-centric factor graph is extended with n new to-be-estimated state variables in each procedure. We extend the graph with n state variables and create GP motion prior factors that constrain the relative state transitions between two successive state variables. In doing so, the timestamps of all state variables are chosen deterministically. While solving the iterative optimization problem, an initial prediction $x_k^- \in \mathcal{X}^-$ must be provided for each state variable. These predictions can be acquired using prior motion models (e.g., GP state extrapolation [48]). In this work, we utilize state propagation using IMU measurements to calculate the initial estimate of future states at high frequency.

As new sensor observations are received at different timestamps in parallel to state estimation, we retrieve the cached m observations from each sensor $s \in \mathcal{S}$ in a second loop. We define a time threshold t_{sync} for state-observation alignment to query the index of related state variables. If state variables can be associated with sensor observations within this threshold, normal sensor factors are added to the graph. Otherwise,

Algorithm 1: Time-centric factor graph optimization

Input : Last state id and timestamp pair (x_{id}^-, x_{ts}^-)
 Propagated states $x_k^- \in \mathcal{X}^-$, $k = 1 \dots n$
 List of sensor measurements $s \in \mathcal{S}$

Output: Current state id and timestamp pair (x_{id}^+, x_{ts}^+)
 Optimized state x_k^+ and uncertainties P_k^+

```

1  $\mathcal{G} \leftarrow \text{initGraph}(x_0^-, P_0^-)$ ;
2 List of state id and timestamp pairs  $\mathcal{P} = \emptyset$ ;
3  $x_{id} = x_{id}^-$ ;
4 for  $k = 1 : n$  do
5    $x_{id}^+ = x_{id} + 1$ ;
6    $x_{ts}^+ = \text{updateTimestamp}(x_{ts}^-)$ ;
7    $\mathcal{G} \leftarrow \text{NewStateVariable}(x_{id}, x_{ts}, \mathcal{X})$ ;
8    $\mathcal{G} \leftarrow \text{GPMotionFactor}(x_{id-1}, x_{id})$ ;
9    $\mathcal{P} \leftarrow (x_{id}, x_{ts})$ ;
10 end for
11 for Each sensor  $s \in \mathcal{S}$  do
12   for Each observation  $k = 1 : m$  do
13      $(x_i^{id}, x_i^{ts}, \tau, \text{type})$ 
14      $\leftarrow \text{queryStateInfo}(\text{timestamp}_k^s, \mathcal{P})$ ;
15     if type is DROPPED then
16       /* Measurements in the past. */;
17        $\text{discardMeasurement}(\mathbf{o}_k^s)$ ;
18     else if type is SYNCHRONIZED then
19        $\mathcal{G} \leftarrow \text{SensorFactor}(x_{id}, \mathbf{o}_k^s)$ ;
20     else if type is INTERPOLATED then
21        $\mathcal{G} \leftarrow$ 
22        $\text{GPSensorFactor}(x_i^{id}, x_{i+1}^{id}, \tau, \mathbf{o}_k^s)$ ;
23     else if type is CACHED then
24       /* Measurements in the future. */
25        $\text{cacheMeasurement}(\mathbf{o}_k^s)$ ;
26   end for
27 end for
28  $\{x_k^+, P_k^+\} \leftarrow$ 
29    $\text{doOptimizationAndMarginalization}(\mathcal{G})$ ;
30 return  $\{(x_{id}^+, x_{ts}^+), x_k^+, P_k^+\}$ 

```

we construct the measurement factors by querying a GP interpolated state aligned with the measurement timestamp. In this case, two successive state variables x_i and x_j , $j = i + 1$ are obtained with a time offset τ between the measurement and the former state x_i .

After graph construction, we employ a Gauss-Newton-like optimizer to solve the MAP problem [49]. The optimized state x_k^+ and marginalized uncertainties P_k^+ are returned for further state propagation, as introduced in Sec. V-E.

IV. MATHEMATICAL BACKGROUND

A. Frames

In this article, we consider the following frames for state representation and illustrate them in Fig. 4:

- 1) *World Geodetic System (WGS84) frame:* The WGS84 frame presents the vehicle's coordinates (latitude φ , longitude λ , and height h) in a unified geodetic system [50]. In this work, we transform the position into the WGS84

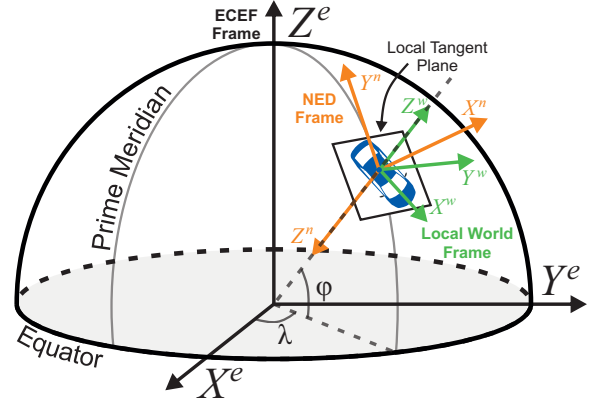


Figure 4: Coordinate frames used in this work.

frame for visualization and do not consider projected coordinate systems to avoid coordinate distortions.

- 2) *Earth-Centered, Earth-Fixed (ECEF) frame:* The ECEF frame, denoted as $(\cdot)^e$, formulates a Cartesian coordinate system at the center of Earth's mass and can be transformed into the WGS84 frame in closed form. We define the pose and velocity of our system in the ECEF frame for the sake of convenience.
- 3) *Navigation frame:* As the vehicle is moving in a local tangent plane on Earth, the north-east-down (NED) frame and the east-north-up (ENU) frame are commonly used as navigation frames $(\cdot)^n$ to present the vehicle's velocity and orientation in planning and control tasks [17]. In this work, vehicle velocity and rotation are transformed into the frame $(\cdot)^n$ for error metrics in experimental studies.
- 4) *Local World Frame:* As shown in [2, 32], odometry information acquired by local sensors (e.g., camera or lidars) refers to an arbitrary local tangent frame that is determined on system initialization with respect to an initial vehicle pose in the navigation frame. We denote this frame as a local world frame $(\cdot)^w$.
- 5) *Body Frame:* We denote the body frame aligned with the IMU sensor center as $(\cdot)^b$. The body frame also represents the local pose $\eta(t)$ of the GP motion models.

B. Notation

To present the state variables in different frames, we use R_b^e and t_b^e to denote the rotational and translational parts from frame b to frame e . This notation is extended as $R_{b,t}^e$ to represent the states with respect to time t . For motion increments in the same frame, we simplify the notation as Δt_{ij} to represent the translational offset of two timestamps i and j . We follow the pose representation $T_b^e = \begin{bmatrix} R_b^e & t_b^e \\ 0 & 1 \end{bmatrix} \in SE(3)$ to calculate the motion increment [51]. For high-dimensional transition matrices in GP motion models (e.g., $\Lambda(\tau) \in \mathbb{R}^{18 \times 18}$), we denote the subblocks $\Lambda_{mn} \in \mathbb{R}^{6 \times 6}$ associated with different state components for linear state querying in (16).

C. Continuous-Time Trajectory Representation using GP

Barfoot et al. [44] originally proposed a continuous-time trajectory representation using Gaussian process regression, which presents an exactly sparse kernel by assuming the system dynamics follow a linear time-varying stochastic differential equation (LTV-SDE):

$$\begin{aligned}\dot{\gamma}(t) &= \mathbf{A}\gamma(t) + \mathbf{B}\mathbf{u}(t) + \mathbf{F}\mathbf{w}(t), \\ \mathbf{w}(t) &\sim \mathcal{GP}(\mathbf{0}, \mathbf{Q}_c \cdot \delta(t - t')), \end{aligned} \quad (1)$$

where the vector $\gamma(t)$ represents a local state variable. The time-varying system matrices are denoted as \mathbf{A} , \mathbf{B} and \mathbf{F} , respectively. The input vector $\mathbf{u}(t)$ is set to $\mathbf{0}$. The process noise $\mathbf{w}(t)$ is given as a zero-mean Gaussian process (GP) with the kernel function formulated with the power spectral density matrix $\mathbf{Q}_c \in \mathbb{R}^{6 \times 6}$ and the Dirac delta function, δ .

In discrete time, this state-space model can be furthermore interpreted to interpolate an arbitrary state at timestamp t_τ ($t_i < t_\tau < t_j$) given an initial local state γ_i using

$$\gamma_i(t_\tau) = \mathbf{\Lambda}(t_\tau)\gamma_i(t_i) + \mathbf{\Omega}(t_\tau)\gamma_i(t_j), \quad (2)$$

where

$$\mathbf{\Lambda}(t_\tau) = \mathbf{\Phi}(t_\tau, t_i) - \mathbf{\Omega}(t_\tau)\mathbf{\Phi}(t_\tau, t_j), \quad (3)$$

$$\mathbf{\Omega}(t_\tau) = \mathbf{Q}_{i,t_\tau}\mathbf{\Phi}(t_\tau, t_j)^T\mathbf{Q}_{i,j}^{-1}. \quad (4)$$

The system transition matrix $\mathbf{\Phi}$ in (3) and (4) can be defined using a white-noise-on-acceleration (WNOA, a.k.a., constant-velocity) prior, as demonstrated in earlier works [44, 52]. Later, Tang et al. [12] introduced a white-noise-on-jerk (WNOJ) prior that presents third-order system dynamics with the system transition function

$$\mathbf{\Phi}(t, t_i) = \begin{bmatrix} \mathbf{1} & (t_i - t)\mathbf{1} & \frac{1}{2}(t_i - t)^2\mathbf{1} \\ \mathbf{0} & \mathbf{1} & (t_i - t)\mathbf{1} \\ \mathbf{0} & \mathbf{0} & \mathbf{1} \end{bmatrix}. \quad (5)$$

The time-varying covariance matrix $\mathbf{Q}_i(t) \in \mathbb{R}^{18 \times 18}$ and its precision matrix $\mathbf{Q}_i^{-1}(t)$ are computed as

$$\mathbf{Q}_i(t) = \begin{bmatrix} \frac{1}{20}\Delta t_i^5\mathbf{Q}_c & \frac{1}{8}\Delta t_i^4\mathbf{Q}_c & \frac{1}{6}\Delta t_i^3\mathbf{Q}_c \\ \frac{1}{8}\Delta t_i^4\mathbf{Q}_c & \frac{1}{3}\Delta t_i^3\mathbf{Q}_c & \frac{1}{2}\Delta t_i^2\mathbf{Q}_c \\ \frac{1}{6}\Delta t_i^3\mathbf{Q}_c & \frac{1}{2}\Delta t_i^2\mathbf{Q}_c & \Delta t_i\mathbf{Q}_c \end{bmatrix}, \quad (6)$$

$$\mathbf{Q}_i^{-1}(t) = \begin{bmatrix} 720\Delta t_i^{-5}\mathbf{Q}_c^{-1} & -360\Delta t_i^{-4}\mathbf{Q}_c^{-1} & 60\Delta t_i^{-3}\mathbf{Q}_c^{-1} \\ -360\Delta t_i^{-4}\mathbf{Q}_c^{-1} & 192\Delta t_i^{-3}\mathbf{Q}_c^{-1} & -36\Delta t_i^{-2}\mathbf{Q}_c^{-1} \\ 60\Delta t_i^{-3}\mathbf{Q}_c^{-1} & -36\Delta t_i^{-2}\mathbf{Q}_c^{-1} & 9\Delta t_i^{-1}\mathbf{Q}_c^{-1} \end{bmatrix}. \quad (7)$$

Compared to other approaches, trajectory representation (interpolation) using Gaussian process regression effectively incorporates physics-driven models to retrieve realistic vehicle motion by scaling the transition function with the time-varying covariance matrix \mathbf{Q} . As the hyper-parameter \mathbf{Q}_c can be tuned for different applications [53], this approach can be extended for nonlinear problems (see Sec. IV-D) and enables more accurate state interpolation [7, 47].

D. GP-WNOJ Motion Prior Model

Following the approach in [12], a GP motion prior for $SE(3)$ can be defined as

$$\begin{aligned}\dot{\mathbf{T}}(t) &= \boldsymbol{\varpi}(t)^\wedge \mathbf{T}(t), \\ \dot{\boldsymbol{\varpi}}(t) &= \mathbf{w}(t), \end{aligned} \quad (8)$$

where the vehicle pose in the global frame is denoted as $\mathbf{T}(t)$, which can be calculated as $\mathbf{T}(t) = \exp(\boldsymbol{\xi}(t)^\wedge)$ with local pose $\boldsymbol{\xi}(t) = [\boldsymbol{\rho}(t)^T \boldsymbol{\phi}(t)^T]^T \in \mathbb{R}^6$. The vectors $\boldsymbol{\rho}(t)$ and $\boldsymbol{\phi}(t)$ represent the position and orientation of a local pose (e.g., in the body frame) [54]. A local pose can be converted to $\mathfrak{se}(3)$ by applying the operator $(\cdot)^\wedge$. The operator $(\cdot)^\vee$ is the inverse of $(\cdot)^\wedge$ [51]. The vector $\boldsymbol{\varpi}(t) = [\boldsymbol{\nu}(t)^T \boldsymbol{\omega}(t)^T]^T \in \mathbb{R}^6$ represents the body-centric velocity. With this motion prior, the state of the GP motion model in a global frame is given as

$$\mathbf{x}(t) = \{\mathbf{T}(t), \boldsymbol{\varpi}(t), \dot{\boldsymbol{\varpi}}(t)\} \in SE(3) \times \mathbb{R}^{12}. \quad (9)$$

However, the GP motion prior in (8) cannot be implemented directly using (1) due to nonlinearity of the system dynamics. To address this problem, Anderson and Barfoot [52] showed that a local linear GP prior can be defined between each state-timestamp pair, t_i and t_{i+1} , by transforming the global pose $\mathbf{T}(t)$ into the local tangent frame, where a local pose $\boldsymbol{\xi}(t)$ can be calculated as

$$\boldsymbol{\xi}_i(t) = \ln(\mathbf{T}(t)\mathbf{T}_{t_i}^{-1})^\vee, \quad t_i \leq t \leq t_{i+1}, \quad (10)$$

where we consider the pose \mathbf{T}_{t_i} at the timestamp t_i as a fixed parameter while formulating the local pose $\boldsymbol{\xi}_i(t)$ for an arbitrary pose $\mathbf{T}(t)$ for $t > t_i$.

Because the motion between state-timestamp pairs, which are usually associated with high-frequency measurement timestamps (e.g., lidar at 10 Hz), is generally small, this local GP prior approximately represents a linear, time-invariant (LTI) SDE, which can be driven from (1) by assuming the system matrices remain constant. Thus, a local state variable of GP-WNOJ prior for $SE(3)$ can be defined as

$$\boldsymbol{\gamma}(t) = [\boldsymbol{\xi}(t)^T \dot{\boldsymbol{\xi}}(t)^T \ddot{\boldsymbol{\xi}}(t)^T]^T \quad (11)$$

and propagated using (2) to (4). The time derivatives of the local pose can be calculated as

$$\dot{\boldsymbol{\xi}}(t) = \mathcal{J}(\boldsymbol{\xi}_i(t))^{-1}\boldsymbol{\varpi}(t), \quad (12)$$

$$\ddot{\boldsymbol{\xi}}(t) = -\frac{1}{2}(\mathcal{J}(\boldsymbol{\xi}(t))^{-1}\boldsymbol{\varpi}(t))^\wedge \boldsymbol{\varpi}(t) + \mathcal{J}(\boldsymbol{\xi}(t))^{-1}\dot{\boldsymbol{\varpi}}(t), \quad (13)$$

where the matrix \mathcal{J} is the left Jacobian of $SE(3)$ [51]. To calculate $\frac{d(\mathcal{J}^{-1})}{dt}$ in closed form for (13), we approximately formulate $\mathcal{J}^{-1} \approx \mathbf{1} - \frac{1}{2}\boldsymbol{\xi}^\wedge$ [12]. The operator $(\boldsymbol{\xi})^\wedge$ represents the adjoint of $\boldsymbol{\xi}^\wedge \in \mathfrak{se}(3)$ [51], which can be calculated as

$$\boldsymbol{\xi}^\wedge = \begin{bmatrix} \boldsymbol{\rho} \\ \boldsymbol{\phi} \end{bmatrix} = \begin{bmatrix} \boldsymbol{\phi}^\wedge & \boldsymbol{\rho}^\wedge \\ \mathbf{0} & \boldsymbol{\phi}^\wedge \end{bmatrix}. \quad (14)$$

Because the left Jacobian requires several matrix calculations, it can be approximated as an identity matrix $\mathbf{1}$ over small intervals to improve the computation efficiency⁴ [55].

⁴We implement this trick as a configuration in the proposed GNSS-FGO.

Given a local state variable that represents the origin system state for each state-timestamp pair, we can retrieve the WNOJ motion model for two successive local state variables in the local frame as

$$\begin{aligned}\gamma_i(t_i) &= [\mathbf{0} \ \varpi(t)^T \ \dot{\varpi}(t)^T]^T, \\ \gamma_i(t_{i+1}) &= \begin{bmatrix} \ln(\mathbf{T}_{i+i,i})^\vee \\ \mathcal{J}_{i+1}^{-1} \varpi_{i+1} \\ -\frac{1}{2}(\mathcal{J}_{i+1}^{-1} \varpi_{i+1})^\wedge \varpi_{i+1} + \mathcal{J}_{i+1}^{-1} \dot{\varpi}_{i+1} \end{bmatrix}. \quad (15)\end{aligned}$$

Using the GP-WNOJ prior, a state at an arbitrary time $\tau \in (i, i+1)$ can be queried as

$$\begin{aligned}\mathbf{T}_\tau &= \exp \left\{ [\Lambda_{12}(\tau) \varpi_i + \Omega_{13}(\tau) \dot{\varpi}_i + \Sigma_{11}(\tau) \ln(\mathbf{T}_{i+i,i})^\vee + \right. \\ &\quad + \Omega_{12}(\tau) \mathcal{J}_{i+1}^{-1} \varpi_{i+1} + \\ &\quad \left. + \Omega_{13}(\tau) (-\frac{1}{2}(\mathcal{J}_{i+1}^{-1} \varpi_{i+1})^\wedge \varpi_{i+1} + \mathcal{J}_{i+1}^{-1} \dot{\varpi}_{i+1})]^\wedge \right\} \mathbf{T}_i, \quad (16)\end{aligned}$$

where Λ and Ω are vehicle transition matrices obtained from (2) to (6).

Remark 1. As discussed in [12], representing a realistic system transition using the GP motion priors requires proper tuning of the power spectral density matrix \mathbf{Q}_c . In this work, we assume that \mathbf{Q}_c is a constant diagonal matrix defined as $\mathbf{Q}_c = \text{diag}(\mathbf{q}_c)$ with a 6D hyper-parameter \mathbf{q}_c . For a fair evaluation of the GP-WNOA and GP-WNOJ models, we do not tune this hyper-parameter explicitly in each test sequence. We formulate \mathbf{Q} in both GP models with the same parameterization for pose weighting.

E. Measurement Models

1) *GNSS Observations:* Generally, a single antenna GNSS receiver can provide both position, velocity, and time (PVT) solutions and raw observations. As the pose and velocity of the PVT solution can be directly associated with the state variables in the FGO, we only present the measurement models for the raw GNSS observations: pseudorange ρ and Doppler shift (a.k.a., deltarange) ν .

In localization approaches that tightly fuse the GNSS observations, pseudorange and deltarange are commonly used and well studied [17]. The pseudorange ρ represents a geometric distance between the phase center of the GNSS antenna and the associated satellite, which is calibrated in a pre-processing step to eliminate satellite orbit bias and atmospheric delays, as shown in [7, 56]. After pre-processing, the pseudorange can be calculated with respect to the antenna position as

$$\tilde{\rho}_k = \|\mathbf{t}_a^e - \mathbf{t}_{\text{sat},k}^e\|_2 + c_b + \delta\rho_M + w_\rho, \quad (17)$$

where the vector \mathbf{t}_a^e and $\mathbf{t}_{\text{sat},k}^e$ represent the positions of GNSS antenna and k -th satellite in ECEF frame, respectively. The variable c_b represents the receiver clock bias for the corresponding satellite source. The measurement noise is denoted as w_ρ . The multi-path error $\delta\rho_M$ is neglected in this work. We filter out all GNSS observations from satellites with an elevation angle less than 15° .

⁵This is an ad-hoc choice, generally used in ground vehicle navigation.

The deltarange ν , or Doppler velocity, is measured as the internal carrier frequency change of the GNSS receiver while moving relative to the corresponding satellite. With this observation, the vehicle velocity concerning the satellite velocity can be represented as

$$\tilde{\nu}_k = (\mathbf{e}_{\text{sat},k}^e)^T (\mathbf{v}_{\text{sat},k}^e - \mathbf{v}_a^e) + c_d + w_{\nu,k}. \quad (18)$$

In (18), the unit vector $\mathbf{e}_{\text{sat},k}^e$ represents the direction from the antenna to the k -th satellite. We denote the satellite and antenna velocities in the ECEF frame as $\mathbf{v}_{\text{sat},k}^e$ and \mathbf{v}_a^e , respectively. The receiver clock drift and measurement noise are given as c_d and $w_{\nu,k}$.

2) *Lidar Odometry:* We adapt the feature extraction and matching methods from a feature-based lidar odometry [2, 13] to obtain the relative motion increments between two laser keyframes. The coordinates of raw lidar points acquired in different timestamps are re-calibrated using the IMU measurement to the original timestamp of the lidar scan. We classify the calibrated points into edge and planar features, $\mathbf{F}_t = \{\mathbf{F}_t^e, \mathbf{F}_t^p\}$, based on the smoothness metric shown in [13, 57]. In scan registration, all k features in \mathbf{F}_{t+1} of the current scan are associated with pose priors $\mathbf{T}_{t+1,1:k}^w$ and used to find the best transformation $\Delta\mathbf{T}_{t,t+1}^w$ from the last laser scan by solving an optimization problem that takes the distance between the corresponding features in \mathbf{F}_t using a Gauss-Newton algorithm.

In [2], a lidar-centric SLAM approach is presented that optionally fuses GPS positioning. This approach can only present accurate state estimates if the scan registration converges and sufficient global references (e.g., GPS position or loop closure) are available. In contrast to [2], we query the vehicle states at scan timestamps from a previously built time-centric graph and integrate the transformation $\Delta\tilde{\mathbf{T}}_{t,t+1}^w$ as between-pose constraints. After the graph optimization, we query the optimized states again using the GP motion model and update lidar keyframe poses in frame w using the following transformation

$$\mathbf{T}_{l,t}^w = \mathbf{T}_{l,\text{anc}}^{e,-1} \mathbf{T}_{l,t}^e, \quad (19)$$

where the transformation matrices $\mathbf{T}_{l,t}^e$ and $\mathbf{T}_{l,t}^w$ denote lidar poses in frame e and frame w , respectively. As lidar odometry requires a state-space representation in a local-world (a.k.a., local-tangent) frame w where the z -axis is gravity aligned, we query an anchor pose $\mathbf{T}_{l,\text{anc}}^e = \begin{bmatrix} \mathbf{R}_{l,\text{anc}}^e & \mathbf{t}_{l,\text{anc}}^e \\ \mathbf{0} & 1 \end{bmatrix}$ of the lidar sensor on first scan and initialize a local-world frame of the lidar odometry by setting the anchor pose as its origin. In contrast to [32], a coarse orientation estimation is unnecessary in our work to align the local-world frame and the navigation frame because the vehicle orientation is given.

3) *Optical Speed Sensor:* We employ a high-grade vehicle optical speed sensor that provides unbiased 2D velocity observations $\bar{\mathbf{v}}_t^b$ in the body frame at 100 Hz. The 2D velocity observations can be associated with the vehicle velocity in the state vector using

$$\tilde{\mathbf{v}}_t^b = \begin{bmatrix} \tilde{v}_{t,x}^b \\ \tilde{v}_{t,y}^b \end{bmatrix} = \begin{bmatrix} 1 & 0 & 0 \\ 0 & 1 & 0 \end{bmatrix} \cdot \mathbf{R}_e^b \mathbf{v}_b^e, \quad (20)$$

where the vector $\tilde{\mathbf{v}}_t^b$ represents the observed 2D velocity components in frame b , which can be evaluated with the vehicle velocity variable \mathbf{v}_b^e transformed with the inverse rotation matrix \mathbf{R}_e^b back to frame b .

V. FGO FOR VEHICLE LOCALIZATION

This section presents our implementation of the proposed GNSS-FGO for two sensor fusion schemes. In loosely coupled fusion, we obtain a baseline trajectory of our datasets by fusing the GNSS-PVT solution with the observed 2D vehicle velocity from a high-grade speed sensor and the lidar odometry. To defend the superiority of fusing raw GNSS observations for vehicle localization, we propose a tightly coupled fusion of raw GNSS observations with IMU measurements and lidar odometry, which is evaluated with the baseline trajectory. In this section, we introduce all probabilistic factor formulations and the proposed factor graph structures.

A. State Variables

The state variable at timestamp t in this work is defined as

$$\mathbf{x}_t \triangleq \{\mathbf{T}_{b,t}^e \ \mathbf{v}_{b,t}^e \ \mathbf{b}_{b,t}^a \ \mathbf{b}_{b,t}^g \ \mathbf{c}_t^r\}. \quad (21)$$

We estimate the vehicle pose $\mathbf{T}_{b,t}^e \in SE(3)$ and 6D velocity \mathbf{v}_b^e in frame e . The vectors $\mathbf{b}_{b,t}^a$ and $\mathbf{b}_{b,t}^g$ denote the 3D biases of the accelerometer and gyroscope, respectively. The 2D vector $\mathbf{c}_t^r = [c_{b,t} \ c_{d,t}]^T$ represents the GNSS receiver clock bias $c_{b,t}$ and drift $c_{d,t}$, which is only estimated by the tightly coupled fusion of raw GNSS observations.

Remark 2. Unlike [12], we do not estimate 6D accelerations in GP motion models to reduce the dimension of the state vector. Instead, we consider the vehicle accelerations measured by the IMU as inputs to the WNOJ model.

B. Factor Formulations

1) *Pre-Integrated IMU Factor:* In graph-optimization-based state estimation approaches, the IMU pre-integration, introduced in [58, 59], is generally utilized to integrate high-frequency IMU measurements as between-state factors for the optimization procedures running at a lower rate. The pre-integrated IMU measurements represent the relative motion increments on manifold. These relative motion increments can be assumed unchanged while re-linearizing the consecutive state variables in the optimization iterations, resulting in efficient computation. Following [59], we define the error function of the IMU factor between two consecutive state variables at timestamps t_i, t_j as

$$\|\mathbf{e}_{ij}^{\text{imu}}\|^2 = \left\| [\mathbf{r}_{\Delta \mathbf{R}_{ij}}^T \ \mathbf{r}_{\Delta \mathbf{v}_{ij}}^T \ \mathbf{r}_{\Delta \mathbf{t}_{ij}}^T]^T \right\|_{\Sigma^{\text{imu}}}^2, \quad (22)$$

where

$$\mathbf{r}_{\Delta \mathbf{R}_{ij}} = (\Delta \tilde{\mathbf{R}}_{ij}(\mathbf{b}_i^g))^{\vee} \mathbf{R}_i^T \mathbf{R}_j, \quad (23)$$

$$\mathbf{r}_{\Delta \mathbf{v}_{ij}} = \mathbf{R}_i^T (\mathbf{v}_j - \mathbf{v}_i - \mathbf{g} \Delta t_{ij}) - \Delta \tilde{\mathbf{v}}_{ij}(\mathbf{b}_i^g, \mathbf{b}_i^a), \quad (24)$$

$$\mathbf{r}_{\Delta \mathbf{t}_{ij}} = \mathbf{R}_i^T (t_j - t_i - \mathbf{v}_i \Delta t_{ij} - \frac{1}{2} \mathbf{g} \Delta t_{ij}^2) - \Delta \tilde{\mathbf{t}}_{ij}(\mathbf{b}_i^g \ \mathbf{b}_i^a). \quad (25)$$

In (23) to (25), we omit the bias derivatives that can be ignored between two state variables. The motion increments $\{\Delta \tilde{\mathbf{R}}_{ij}, \Delta \tilde{\mathbf{v}}_{ij}, \Delta \tilde{\mathbf{t}}_{ij}\}$ are provided by the IMU pre-integration with

$$\Delta \tilde{\mathbf{R}}_{ij} = \prod_{k=i}^{j-1} ((\tilde{\omega}_k - \mathbf{b}_i^g) \Delta t)^\wedge, \quad (26)$$

$$\Delta \tilde{\mathbf{v}}_{ij} = \sum_{k=i}^{j-1} \Delta \tilde{\mathbf{R}}_{ik} (\tilde{\mathbf{a}}_k - \mathbf{b}_i^a) \Delta t, \quad (27)$$

$$\Delta \tilde{\mathbf{t}}_{ij} = \sum_{k=i}^{j-1} \left[\Delta \mathbf{v}_{ik} \Delta t + \frac{1}{2} \Delta \tilde{\mathbf{R}}_{ik} (\tilde{\mathbf{a}}_k - \mathbf{b}_i^a) \Delta t^2 \right], \quad (28)$$

where the raw vehicle acceleration $\tilde{\mathbf{a}}$ and rotation rate $\tilde{\omega}$ from the IMU are integrated. The pre-defined noise parameters $\{\eta_a, \eta_g\}$ are propagated to acquire the covariance matrix Σ^{imu} [58]. The gravity vector is updated according to the current position in the e frame for each pre-integration.

As in [58], we estimate the accelerometer and gyroscope biases with the Brownian motion model by formulating the bias error function as

$$\|\mathbf{e}_{ij}^b\|^2 = \|\mathbf{b}_j^a - \mathbf{b}_i^a\|_{\Sigma^a}^2 + \|\mathbf{b}_j^g - \mathbf{b}_i^g\|_{\Sigma^g}^2. \quad (29)$$

2) *Between-Pose Factor:* For the relative odometry observations $\Delta \tilde{\mathbf{T}}_{i,j}^e = \{\Delta \tilde{\mathbf{R}}_{i,j}^e \ \Delta \tilde{\mathbf{p}}_{i,j}^e\}$, we follow the original implementation in [60] and formulate the between pose factor represented as

$$\|\mathbf{e}_{i,j}^{\text{bp}}\|^2 = \left\| \ln(\mathbf{T}_i^{e,-1} \mathbf{T}_j^e \Delta \tilde{\mathbf{T}}_{i,j}^e)^\vee \right\|_{\Sigma^{\text{bp}}}^2, \quad (30)$$

where the pose \mathbf{T}_i^e and \mathbf{T}_j^e are queried using timestamps associated with two successive lidar scans.

3) *Velocity Factor:* We use the 2D observations $\tilde{\mathbf{v}}_t^b$ to formulate the navigation velocity factor. As the measured velocity can be directly associated with the velocity in state variables, as denoted in (20), we formulate the error function for the velocity observations considering the lever arm $\mathbf{l}^{b,\text{vel}}$ from the body frame to the sensor center as

$$\|\mathbf{e}_i^{\text{vel}}\|^2 = \left\| \begin{bmatrix} 1 & 0 & 0 \\ 0 & 1 & 0 \end{bmatrix} \cdot (\mathbf{R}_{e,i}^b \mathbf{v}_{b,i}^e + \omega_i^{b \wedge} \mathbf{l}^{b,\text{vel}}) - \tilde{\mathbf{v}}_i^b \right\|_{\Sigma^{\text{vel}}}^2. \quad (31)$$

4) *GNSS-PVT Factor:* We propose a generalized implementation of the GNSS-PVT factor for the observed antenna position $\tilde{\mathbf{t}}_{\text{ant}}^e$ and the velocity $\tilde{\mathbf{v}}_{\text{ant}}^n$. Taking into account the lever arm $\mathbf{l}_{\text{ant}}^b$ from the IMU center to the phase center of the GNSS antenna, we calculate the antenna position at timestamp t_i as $\mathbf{t}_{\text{ant},i}^e = \mathbf{t}_{b,i}^e + \mathbf{R}_{b,i}^e \mathbf{l}_{\text{ant}}^b$ and velocity as $\mathbf{v}_{\text{ant},i}^e = \mathbf{v}_{b,i}^e + \mathbf{R}_{b,i}^e (\omega_i^b)^\wedge \mathbf{l}_{\text{ant}}^b$. Thus, the error function can be derived as

$$\|\mathbf{e}_i^{\text{pvt}}\|^2 = \left\| [\mathbf{r}_{t_i}^T \ \mathbf{r}_{v_i}^T]^T \right\|_{\Sigma^{\text{pvt}}}^2, \quad (32)$$

with

$$\mathbf{r}_{t_i} = \mathbf{t}_{\text{ant},i}^e - \tilde{\mathbf{t}}_{\text{ant},i}^e, \quad (33)$$

$$\mathbf{r}_{v_i} = \mathbf{R}_{e,i}^n \mathbf{v}_{\text{ant},i}^e - \tilde{\mathbf{v}}_{\text{ant},i}^n, \quad (34)$$

where the rotation matrix $\mathbf{R}_{e,i}^n$ can be calculated using the direction cosine matrix with the current geodetic coordinate (φ_i, λ_i) as

$$\mathbf{R}_{e,i}^n = \begin{bmatrix} -\sin \lambda_i & -\cos \lambda_i \sin \varphi_i & \cos \lambda_i \sin \varphi_i \\ \cos \lambda_i & -\sin \lambda_i \sin \varphi_i & \sin \lambda_i \sin \varphi_i \\ 0 & \cos \varphi_i & \sin \varphi_i \end{bmatrix}. \quad (35)$$

5) *Pseudorange and Deltarange (PrDr) Factor*: We derive the error function for the pre-processed pseudorange and deltarange observations with (17) and (18) as

$$\|e_i^{\text{PrDr}}\|^2 = \|[r_i^{\text{Pr}} \ r_i^{\text{Dr}}]^T\|_{\Sigma^{\text{PrDr}}}^2, \quad (36)$$

where

$$r_i^{\text{Pr}} = \|\mathbf{t}_{\text{ant},i}^e - \mathbf{t}_{s,i}^{e,k}\| + c_{b,i} - \tilde{\rho}_i^k, \quad (37)$$

$$r_i^{\text{Dr}} = \mathbf{u}_{\text{ant},i}^{s,k,T} (\mathbf{v}_{\text{ant},i}^e - \mathbf{v}_{s,i}^{e,k}) + c_{d,i} - \tilde{\nu}_i^k. \quad (38)$$

In (37) and (38), the vectors $\mathbf{t}_{s,i}^{e,k}$ and $\mathbf{v}_{s,i}^{e,k}$ are the position and velocity of k -th satellite in frame e , respectively. The unit vector $\mathbf{u}_{\text{ant},i}^{s,k}$ denotes the direction from the antenna to the k -th satellite. The receiver clock bias $c_{b,i}$ and drift $c_{d,i}$ are also evaluated in (36).

We consider a scaled Carrier-to-Noise ratio (C/N_0) with hyper-parameters λ_ρ and λ_ν to represent the variance of pseudorange and deltarange observations, which is denoted as

$$\eta_\rho^2 = \lambda_\rho 10^{-\frac{C/N_0}{10}}, \quad \eta_\nu^2 = \lambda_\nu 10^{-\frac{C/N_0}{10}}. \quad (39)$$

Due to the strong corruption of GNSS observations in urban areas, we use m-Estimator [61] to enhance the optimization robustness by reforming the error function e_i^{PrDr} into

$$\hat{e}_i^{\text{PrDr}} = \phi(e_i^{\text{PrDr}}), \quad (40)$$

where the robust error formulation $\phi(\cdot)$ can be defined with different loss functions such as *Huber* or *Cauchy* [62].

6) *GNSS Receiver Clock Error Factor*: In the tight coupling of the raw GNSS observations, the unknown receiver clock bias and drift (cbd) are estimated in the state variable by assuming a constant drifting model, which can be fused as

$$\|e_i^{\text{cbd}}\|^2 = \left\| \begin{bmatrix} 1 & \Delta t \\ 0 & 1 \end{bmatrix} \begin{bmatrix} c_{b,i-1} \\ c_{d,i-1} \end{bmatrix} - \begin{bmatrix} c_{b,i} \\ c_{d,i} \end{bmatrix} \right\|_{\Sigma^{\text{cbd}}}^2. \quad (41)$$

7) *GP-WNOJ Motion Prior Factor*: We implement the GP-WNOJ motion model as between-state factors, similar to [46]. The error function was originally given in [12] using (15). We summarize this error function for convenience as

$$\|e_{ij}^{\text{gp}}\|^2 = \left\| [\mathbf{r}_{\Delta\gamma_{ij}}^T \ \mathbf{r}_{\Delta\varpi_{ij}}^T]^T \right\|_{\Sigma^{\text{gp}}}^2, \quad (42)$$

where

$$\mathbf{r}_{\Delta\gamma_{ij}} = \ln(\mathbf{T}_{j,i})^\vee - (t_j - t_i)\varpi_i - \frac{1}{2}(t_j - t_i)^2\ddot{\varpi}_i, \quad (43)$$

$$\mathbf{r}_{\Delta\varpi_{ij}} = \mathcal{J}_{j,i}^{-1}\varpi_j - \varpi_i - (t_j - t_i)\ddot{\varpi}_i. \quad (44)$$

As introduced in Sec. V-A, we used the measured accelerations of the IMU in our GP motion models. Thus, only the 6D pose and the 6D velocity are evaluated in GP-WNOJ motion factors, so that $e_{ij}^{\text{gp}} \in \mathbb{R}^{12}$. The analytical Jacobians of the GP motion models can be found in [12, 63].

C. Loosely Coupled FGO

Although the loosely coupled fusion with GNSS and IMU measurements is shown to be less performant compared to tight coupling [6], we implemented a loosely coupled fusion of sensor observations to i) propose a baseline trajectory by integrating a high-grade speed sensor for our dataset in urban areas, where an RTK-fixed GNSS-PVA solution is unreliable; ii) evaluate the loosely and tightly coupled fusion for GNSS-based vehicle localization in challenging areas; iii) demonstrate the flexibility and scalability of the proposed method.

The proposed factor graph is shown in Fig. 5. The states $\mathbf{x}_{1:t}$ are created deterministically on the graph independently of any measurement. If a measurement cannot be associated with any state variable, a state $\hat{\mathbf{x}}_{i+\tau}$ between two state variables $\hat{\mathbf{x}}_i$ and $\hat{\mathbf{x}}_{i+1}$ (where $0 < \tau < 1$) is queried for the error evaluation.

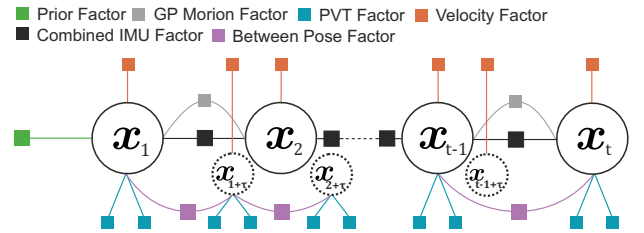


Figure 5: Proposed loosely coupled GNSS-FGO.

The optimization problem can then be formulated as

$$\hat{\mathbf{x}} = \underset{\mathbf{x}}{\operatorname{argmin}} \left(\|e^0\|_{\Sigma^0}^2 + \sum_{i=1}^M \|e_i^{\text{imu}}\|_{\Sigma^{\text{imu}}}^2 + \sum_{i=1}^M \|e_i^{\text{gp}}\|_{\Sigma^{\text{gp}}}^2 + \sum_{i=1}^N \|e_i^{\text{vel}}\|_{\Sigma^{\text{vel}}}^2 + \sum_{i=1}^K \|e_i^{\text{pvt}}\|_{\Sigma^{\text{pvt}}}^2 + \sum_{i=1}^J \|e_i^{\text{bp}}\|_{\Sigma^{\text{bp}}}^2 \right), \quad (45)$$

where the error term e^0 represents the prior factor obtained at initialization or from marginalization. Because sensor observations are received asynchronously other than estimation timestamps M , we use different index notations N , K , J to indicate the number of sensor observations in (45).

D. Tightly Coupled FGO

In contrast to the loosely coupled fusion approach, a tightly coupled fusion of raw GNSS observations contributes more constraints with multiple observed satellites to state variables, as illustrated in Fig. 6. Unlike Fig. 5, we include the pseudorange and deltarange factors in the graph, providing redundant constraints to each state variable. To improve the robustness while GNSS observations are degraded or lost in challenging areas, we include lidar odometry as between-state constraints to improve the consistency of the estimated trajectory. The receiver clock error factor is also added to the graph.

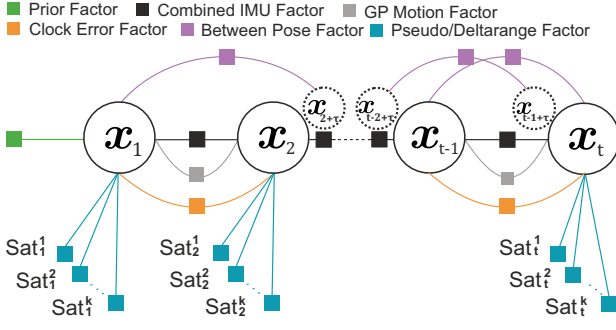


Figure 6: Proposed tightly coupled GNSS-FGO.

The optimization problem with sensor observations from different time domains becomes

$$\begin{aligned} \hat{X} = \operatorname{argmin}_x & \left(\|e_i^0\|_{\Sigma_0}^2 + \sum_{i=1}^M \|e_i^{\text{IMU}}\|_{\Sigma^{\text{IMU}}}^2 + \sum_{i=1}^M \|e_i^{\text{GP}}\|_{\Sigma^{\text{GP}}}^2 \right. \\ & + \sum_{i=1}^N \|e_i^{\text{bp}}\|_{\Sigma^{\text{bp}}}^2 + \sum_{i=1}^M \|e_i^{\text{cbd}}\|_{\Sigma^{\text{cbd}}}^2 + \\ & \left. + \sum_{i=1}^J \sum_{s=1}^K \|\hat{e}_{s,i}^{\text{PrDr}}\|_{\phi(\Sigma^{\text{PrDr}})}^2 \right). \end{aligned} \quad (46)$$

E. System Overview

The system overview with the implementation of Alg. 1 and all data interfaces is shown in Fig. 7. The sensor data are received and pre-processed in separate processes. We construct the time-centric factor graph in a two-stage process, as introduced in Alg. 1. The first stage (line 4-10 of Alg. 1) includes between-state factors and delay-free IMU factors to build a deterministic graph on time. Subsequently, asynchronous sensor observations are fused into the deterministic graph by aligning the timestamps between the measurement and the state variables (line 11-24 of Alg. 1). For measurements that cannot be aligned with any state, two successive state variables are queried to construct a GP-interpolated state for measurement evaluation in optimization procedures. The time-centric graph can be optimized using a fixed-lag batch optimizer [64] or a fixed-lag incremental smoother iSAM2 [65] at a lower frequency. In the experimental results, the estimated trajectories in the error metrics are optimized using iSAM2. We also evaluate both smoothers with respect to both estimator performance and computation efficiency, as presented in Sec. VII-D. After each optimization procedure, we forward the optimized state variables to a state publisher and sensor pre-processing modules. The state publisher is associated with the IMU sensor and provides high-frequent state estimates at 200 Hz.

Remark 3. Near-Zero-Velocity Detection: While the vehicle is stationary, the state estimation exhibits random pose drift. This is a known problem in vehicle localization using inertial measurements [66]. In this case, the state observability degrades dramatically due to insufficient IMU excitation, leading to unbounded error accumulation. Thus, we follow the idea

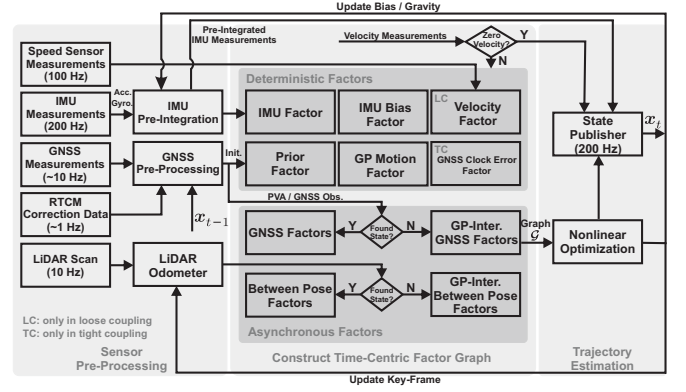


Figure 7: System overview showing all data interfaces and factor types by implementing Alg. 1.

proposed in [66] to detect near-zero velocity motion by voting through multiple sensors that provide velocity information. If the vehicle is voted to be stationary, we temporally pause the graph optimization and state propagation.

F. Implementation

We implemented our approach in C++ using Robot Operating System ROS2⁶. The open-source software library GTSAM⁷ was extended to implement the graph and factor formulations. We adopted the software solution for lidar odometry from LIO-SAM⁷, where only the front-end feature extraction and association were adapted in our work. We used the positioning and orientation estimation solution from a dual-antenna GNSS setup to initialize the state variable x_0 . In this work, we used a laptop with an Intel i9-9900K, 16 cores at max. 4.7 GHz and 64 GB memory for sensor pre-processing and graph optimization in experimental studies.

VI. MEASUREMENT SETUP AND TEST SEQUENCES

A. Measurement Setup

In the measurement campaigns, we recorded sensor data of long-range routes in different areas of Aachen, Düsseldorf and Cologne. Our sensor setup included a dual-antenna GNSS receiver (Novatel PwrPark7D), a Microstrain 3DM-GX5 IMU, and a Velodyne VLP-16 lidar. A high-grade optical speed sensor, Correvit S-Motion DTI from Kistler, was mounted on the trailer hitch at the vehicle's rear side. The test vehicle is shown in Fig. 8.

The IMU data were acquired at 200 Hz, while the GNSS observations and lidar pointclouds were recorded at 10 Hz. We used the high-grade GNSS receiver Novatel PwrPark7D with a dual constellation of GPS and Galileo satellite systems as a reference source. In addition to the sensor data, we received the 1PPS signal at 1 Hz to calculate the measurement delays. The RTCMv3 correction data from German satellite positioning service SAPOS⁹ was also stored at about 1 Hz for GNSS pre-processing.

⁶<https://docs.ros.org/en/rolling/index.html>

⁷<https://gtsam.org>

⁸<https://github.com/TixiaoShan/LIO-SAM>

⁹<http://www.sapos.nrw.de>

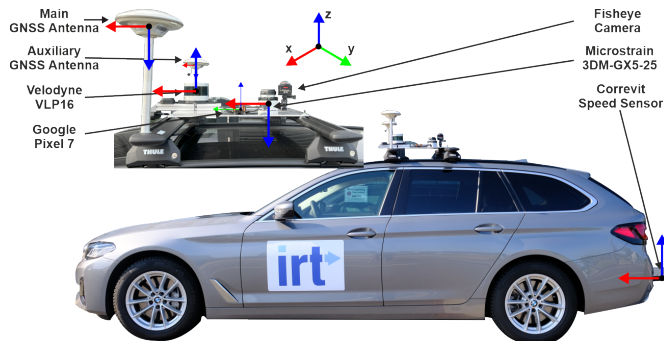


Figure 8: Sensor setup and frames on the test vehicle.

B. Test Sequences

Our dataset contains different driving scenarios: open-sky, semi/dense-urban, and high-speed track. For a clear evaluation, we define different test sequences throughout multiple measurement campaigns and analyze the driving conditions for each sequence, as shown in Table I. The test sequences include lengthy runs with a max. 17km route, aiming to evaluate the estimation performance for long-term operations. For test sequences in urban areas, we chose data from scenarios with different urbanization rates containing tunnel and bridge crossings to evaluate the limitations of the proposed fusion approaches. In addition, we also considered open-sky areas on the high-speed track, where a maximum vehicle speed of 170 km/h was reached, creating significant motion distortion in the lidar point clouds.

Table I: Test sequences definition. We denote the test sequences in Aachen, Düsseldorf, Cologne, and high-speed tracks with “AC”, “DUS”, “C”, and “HS”, respectively. The variable \bar{v} represents the average speed and the scalar $\bar{n}^{\text{sat.}}$ is the average number of satellites used for a GNSS-PVA solution. We calculated the ratio of RTK-fixed solution and No-Solution due to insufficient GNSS observations denoted by $R_{\text{fixed}}^{\text{RTK}}$ and R^{NS} , correspondingly.

Seq.	Leng. (km)	Tunnel (m)	Dura. (s)	\bar{v} (km/h)	$\bar{n}^{\text{sat.}}$	$R_{\text{fixed}}^{\text{RTK}}$ (%)	R^{NS} (%)
AC	17.0	270	2477	27.25	11	76.51	1.7
DUS	5.25	-	1350	13.48	8	52.06	0.9
C01	0.81	276	160	17.89	7	60.8	31.78
C02	1.45	145	390	13.36	7	37.74	11.56
HS	10.6	-	300	124.82	14	94.9	1.47

C. Reference Trajectory and Metrics

To evaluate the proposed fusion strategies, we employ the RTK-fixed GNSS-PVA solution associated with low uncertainties ($\sigma_{\text{pos}} < 0.05\text{m}$ and $\sigma_{\text{rot}} < 1^\circ$) to calculate the absolute root mean square error (RMSE).

Besides the error metrics, we employ Pythagoras’ theorem implemented in the Open Motion Planning Library¹⁰ (OMPL) to calculate the trajectory smoothness (contrary to trajectory roughness) for all test sequences. The smoothness is given as the sum of angles between all path segments in the local-world frame, as denoted in (47), where the variables a_i , b_i and c_i are the length of trajectory segments containing three successive

vehicle positions in the Euclidean frame. For the same test sequence with k vehicle positions, a smaller s shows a large smoothness of the trajectory.

$$s = \sum_{i=2}^{k-1} \left(\frac{2(\pi - \arccos \frac{a_i^2 + b_i^2 - c_i^2}{2a_i b_i})}{a_i + b_i} \right)^2. \quad (47)$$

VII. EXPERIMENTS AND RESULTS

A. Experiment Setting

To evaluate the proposed GNSS-FGO, we first benchmarked the loosely coupled fusion of the GNSS solution with multiple sensor observations using the proposed GNSS-FGO with a lidar-centric SLAM approach LIO-SAM [2], aiming to evaluate the robustness of the proposed method. For a fair evaluation, we have adapted the LIO-SAM implementation⁶ using the same robust error models and parameterizations as in our method. We also enabled loop-closure detection in LIO-SAM to maximize state estimation performance. Later, we conducted experiments by fusing raw GNSS observations alongside IMU and lidar measurements in a tight coupling, which is expected to present more robust trajectory estimation in challenging areas compared to the loose coupling. Lastly, we discussed the smoother type and computation time using different lag sizes. We also evaluated the GP-WNOJ prior with the GP-WNOA prior.

B. General Error Metrics

With pre-defined test sequences in Table I, we present the general error metrics for all experiments in Table II by taking the RTK-fixed GNSS-PVA solution as ground truth. Because an RTK-fixed solution is unavailable in challenging areas, we denote the solution rate used as a ground-truth reference to calculate error metrics of each test sequence in percentage in the column “Seq.”.

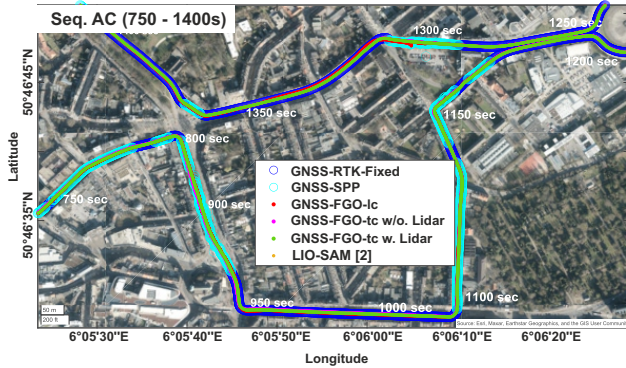
1) *Lidar-Centric Fusion*: As shown in Table II, the lidar-centric SLAM approach LIO-SAM failed in several test sequences even when the same factors with robust error modeling were used and loop-closure detection was enabled (see video demonstration²). The most frequent reason is that scan registration fails due to an invalid feature association, which can be observed in all failed test sequences. Fig. 1a demonstrates this result, where the estimation diverged and cannot be recovered after the vehicle entered a tunnel. In Seq. HS, the lidar-centric approach cannot even be initialized properly while the vehicle was moving very fast, which was not observed in the proposed GNSS-FGO.

We conjecture that because graph construction in [2] requires strict timestamp synchronization of GNSS measurements with lidar timestamps, asynchronous GNSS measurements are dropped, resulting in information loss, and thus, the trajectory smoothness and estimation accuracy are dramatically penalized (see Table II). This hypothesis is supported in the test sequences DUS and C01 (see Fig. 10 and Fig. 11), where the estimated height, orientation, and velocities were frequently diverted.

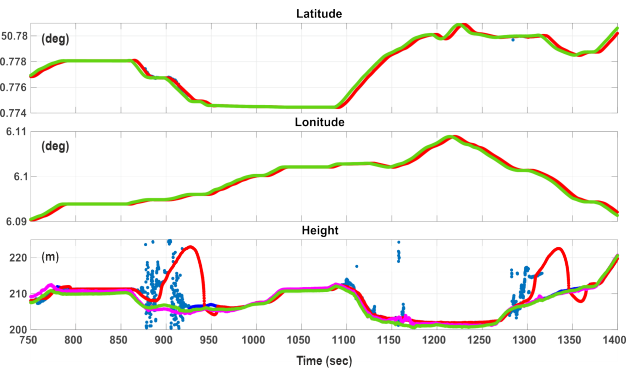
¹⁰<https://ompl.kavrakilab.org/>

Table II: General Trajectory Estimation Metrics. The rate of RTK-fixed GNSS-PVA solution used for the error metrics is denoted in the first column. A test run is classified as failed if the algorithm diverges.

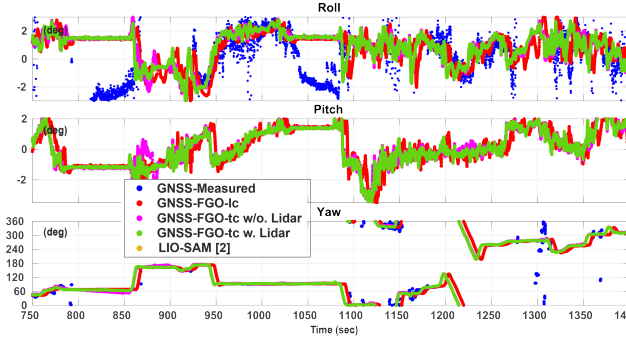
Seq.	Configuration	Mean 2D Pos. Err. (m)	2D Pos. STD (m)	Max. 2D Pos. Err. (m)	Mean 3D Pos. Err. (m)	3D Pos. STD (m)	Max. 3D Pos. Err. (m)	Mean Yaw Err. (°)	Yaw STD (°)	Max. Yaw Err. (°)	<i>s</i>
AC (52%)	LIO-SAM [2]	Failed									
	GNSS-FGO-ic	0.188	0.052	5.653	0.385	0.075	17.61	0.36	1.03	86.14	5108.23
	GNSS-FGO-ic w/o. LiDAR	0.936	0.650	5.877	1.276	1.392	6.127	2.76	2.68	88.53	1706.63
	GNSS-FGO-ic w. LiDAR	0.476	0.738	1.605	1.057	1.088	2.343	1.18	2.13	85.12	982.40
DUS (18%)	LIO-SAM [2]	0.7359	-	9.129	1.024	-	17.391	1.758	-	80.44	2.15e+5
	GNSS-FGO-ic	0.397	0.028	6.821	1.146	0.042	19.36	0.216	0.44	30.64	5672.83
	GNSS-FGO-ic w/o. LiDAR	1.123	1.081	4.415	1.461	2.524	7.141	0.473	3.01	81.32	3595.72
	GNSS-FGO-ic w. LiDAR	1.074	0.921	4.390	2.170	1.890	5.742	0.492	2.74	47.867	3260.06
C01 (57%)	LIO-SAM [2]	3.339	-	8.186	3.478	-	8.463	3.774	-	34.260	6.30e+5
	GNSS-FGO-ic	0.043	0.013	0.875	0.047	0.022	1.271	0.160	0.51	4.069	144.077
	GNSS-FGO-ic w/o. LiDAR	0.516	1.395	0.903	1.223	2.849	2.336	2.134	2.43	7.567	1.52e+5
	GNSS-FGO-ic w. LiDAR	0.402	0.846	0.807	0.468	1.892	0.841	0.888	2.76	7.025	122.358
C02 (27%)	LIO-SAM [2]	Failed									
	GNSS-FGO-ic	0.010	0.010	0.164	0.014	0.023	0.165	0.085	0.79	1.146	2.15e+6
	GNSS-FGO-ic w/o. LiDAR	0.933	1.111	1.933	1.188	2.836	2.104	0.927	4.15	3.811	198.03
	GNSS-FGO-ic w. LiDAR	0.264	1.039	0.499	0.328	2.402	0.565	0.496	2.40	9.716	218.42
HS (78%)	LIO-SAM [2]	Failed on Initialization									
	GNSS-FGO-ic	0.03	0.083	0.944	0.263	0.05	1.562	0.09	0.33	1.57	0.0125
	GNSS-FGO-ic w/o. LiDAR	0.404	0.509	2.265	0.822	1.08	4.833	0.993	1.69	10.05	0.1388
	GNSS-FGO-ic w. LiDAR	0.475	0.672	3.121	1.400	1.252	3.609	0.699	0.94	3.778	0.060



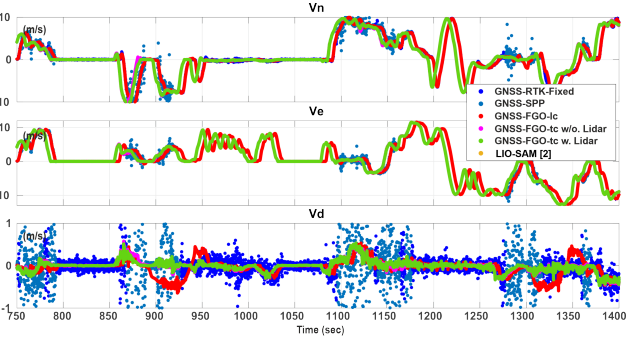
(a) 2D Trajectories of Seq. AC.



(b) Coordinates in the WGS84 frame.



(c) Estimated rotation in the NED frame.



(d) Estimated velocity in the NED frame.

Figure 9: Trajectory plot (700s - 1400s) in urban areas in Aachen. We plot the GNSS single point position (SPP) if the RTK-fixed solution is unavailable.

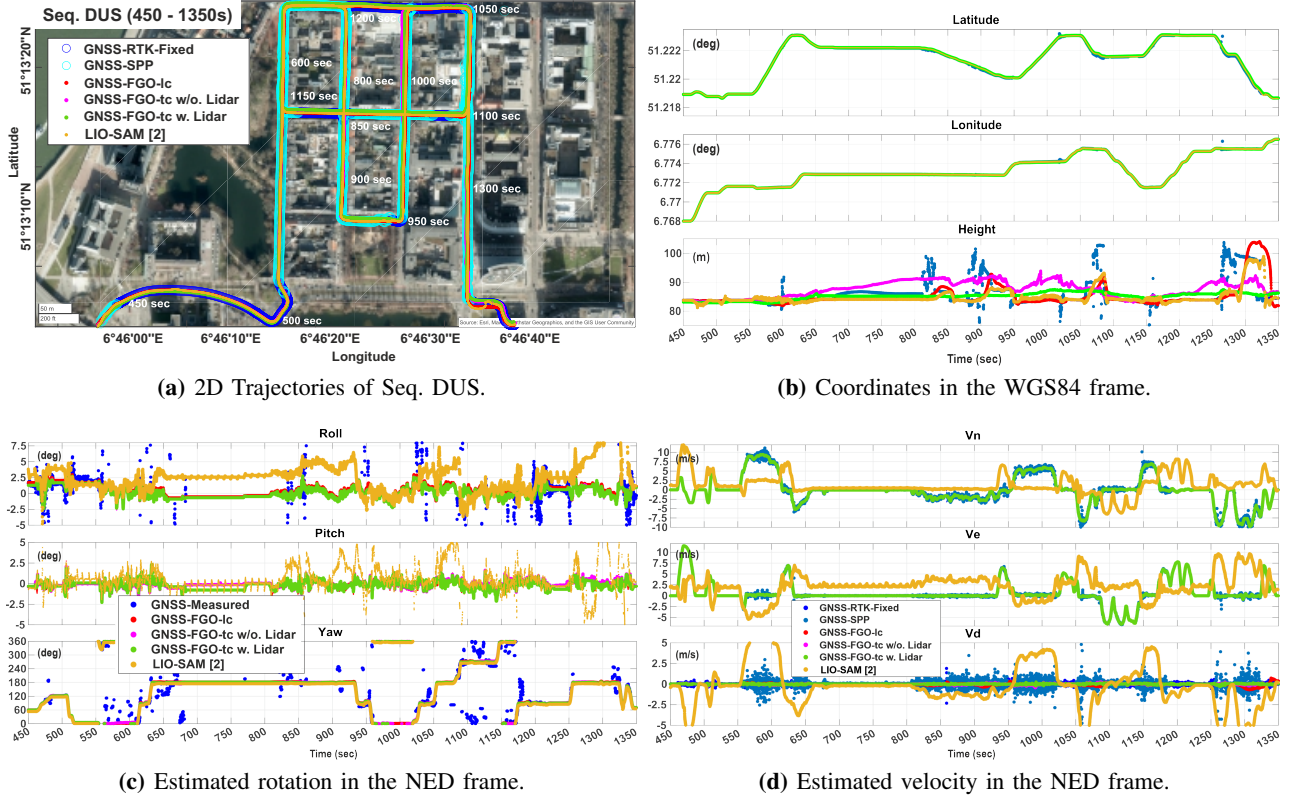


Figure 10: Trajectory plot (450 s - 1350 s) in challenging areas in Düsseldorf.

2) *Loosely Coupled (lc) Fusion*: Because the position and velocity can be directly observed by fusing the GNSS solution in the loose coupling, the to-be-estimated state variables are effectively constrained, resulting in highly accurate trajectory estimation in open-sky areas. For instance, Seq. C01 and C02 present mean position errors less than 5 cm, while the max. position errors remain below 1 m. For long test sequences (e.g., Seg. AC), the loosely coupled fusion using the proposed GNSS-FGO also presents sufficient estimation performance by integrating multiple sensor observations. However, a fast divergence and larger max. position errors can be observed in challenging scenarios using this fusion mechanism. As shown in Fig. 9b and Fig. 10b, the estimated height (in red) diverges significantly once the GNSS positioning is corrupted. This result also proves that the 2D velocity measurements provided by the 2D speed sensor cannot sufficiently constrain the state space. For state variables such as the vertical velocity component v_d^n that are observed with noisy measurements, frequent drifting can be expected (see Fig. 9d). Moreover, the loose coupling generally presents larger trajectory roughness compared to other configurations. Compared to the Seq. AC (see Fig. 9), a higher urbanization rate can be expected in Düsseldorf, leading to an unsmooth trajectory estimation.

3) *Tightly Coupled (tc) Fusion*: Compared to loosely coupled sensor fusion, integrating pre-processed GNSS observations in a tight coupling contributes to redundant state constraints. Thus, the tightly coupled fusion can generally present more robust trajectory estimations with a smaller max.

position error and larger trajectory smoothness in lengthy runs, except in the high-speed scenario (Seq. HS). However, because the vehicle pose and velocity cannot be directly observed with pseudorange and deltarange, lower accuracy can be expected. In challenging urban areas such as Seq. C01 and C02, fusing the lidar odometry as between-state constraints generally improves the estimation performance and trajectory smoothness. This conclusion can also be drawn when referring to Fig. 10b and Fig. 11b, where more accurate height and velocity estimations can be observed by fusing lidar odometry in the graph. In high-speed scenarios, lidar scans suffer from serious motion distortion, and no sufficient features can be extracted compared to urban areas. Therefore, a limited performance improvement can be observed by fusing lidar odometry in the graph.

4) *Discussion*: Based on the experimental results presented above, a robust trajectory estimation can be achieved in challenging scenarios using the proposed approach by fusing multiple sensor measurements, which supports our hypothesis proposed in Sec. II. On the contrary, it can be observed that trajectory drift cannot be effectively eliminated using the classic sensor-centric localization approach LIO-SAM. Even worse, the robustness and reliability of sensor-centric approaches cannot be guaranteed in challenging areas once the primary sensor is compromised. As online applications raise requirements on computation time and resources, sensor degradation due to, e.g., insufficient data processing, becomes nontrivial. The proposed GNSS-FGO presents an effective

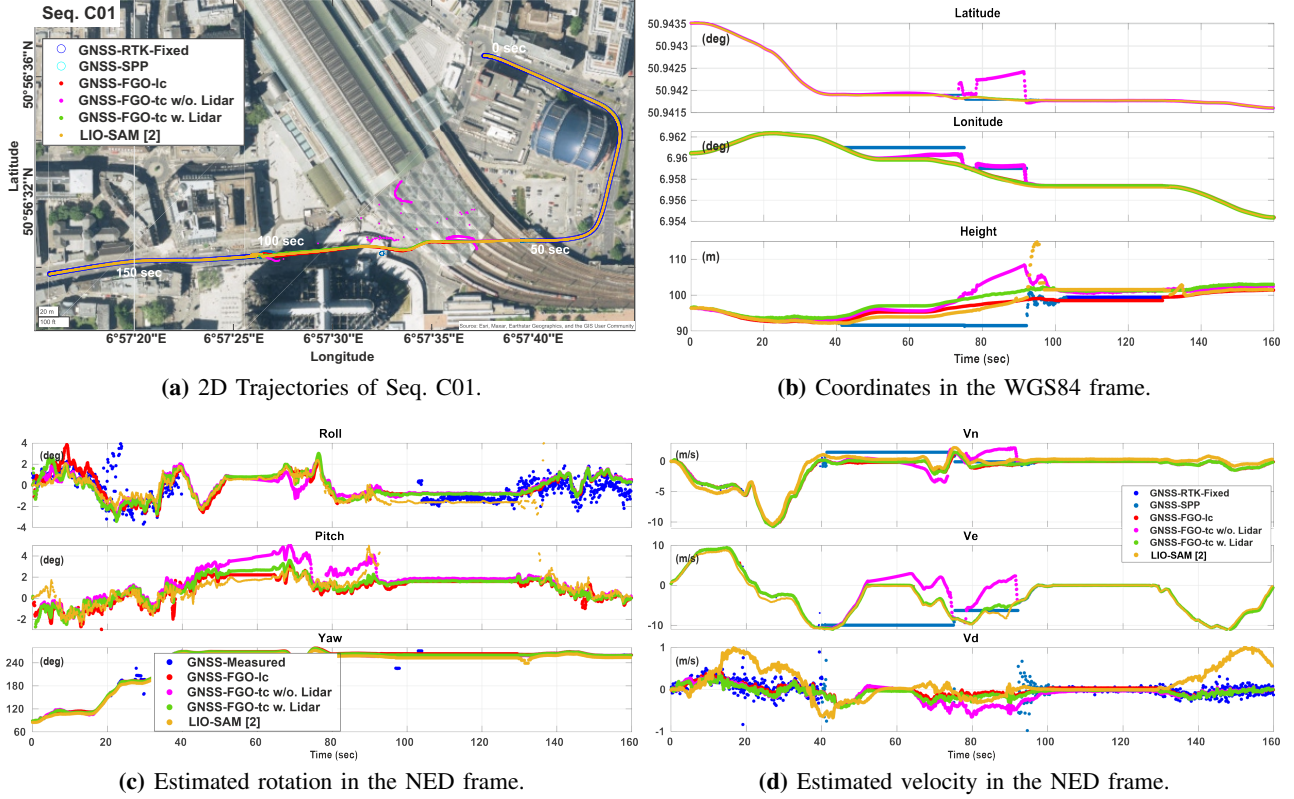


Figure 11: Trajectory plot near the central station of Cologne. For the tightly coupled fusion, we omitted the near-zero-velocity detection in order to present the trajectory drifting while the receiver clock error is unobservable.

workaround while fusing multiple sensors to discharge dependence on a single sensor, which enables lossless information fusion and improves the robustness of the estimation if sensor failure can be expected.

Within GNSS-FGO, loosely fusing the GNSS positioning solution enables fast estimation convergence and higher accuracy in open-sky areas compared to tightly coupled fusion in our study. The loosely coupled fusion diverges quickly once the vehicle enters challenging areas, even when more sensor modalities are integrated. In contrast, the tightly coupled multi-sensor fusion presents a more robust trajectory estimation in our experimental studies. The same conclusion has also been shown in [6, 32]. However, an acceptable accuracy cannot be achieved, especially in dense urban scenarios. For instance, although all estimated trajectories using the proposed GNSS-FGO in Fig. 1 remain consistent, a large drift is presented using the proposed sensor integration. One possible reason can be traced back to lidar degradation and insufficient outlier rejection in GNSS observations. As GNSS-FGO provides a flexible fusion mechanism, this problem can be addressed by integrating more effective state constraints into the graph.

C. Challenging Scenarios

In this part, we propose experimental studies regarding GNSS observations, lidar odometry, and solver settings. We also evaluated the GP-WNOA and GP-WNOJ priors and discussed the hyper-parameter tuning for \mathcal{Q}_c .

1) *Loss of GNSS Observation*: Generally, losing GNSS observations in a short time interval does not lead to immediate divergence or trajectory drift if multiple state constraints such as lidar odometry or motion prior factors are still presented. This conclusion can be drawn from our experiment in Seq. C01, where the vehicle crossed a large bridge at the central train station in Cologne, as shown in Fig. 11. However, fusing GNSS observations in a tight coupling extends the state variables with receiver clock bias and drift $c_r = [c_b \ c_d]^T$, which become unobservable if less than four satellites are visible. Fig. 12 shows the estimated clock bias c_b with respect to the number of received satellites. In the graph where only GNSS observations are integrated, the estimated clock bias drifts dramatically, which is not observed in the graph fused with the lidar odometry. Similar results can also be observed in other experiments, in which the unobservable state variables can lead to estimation divergence and an ill-posed optimization problem. Furthermore, if the global reference (e.g., GNSS observations) is lost over a long time interval, such as crossing a long tunnel, a large trajectory drift can be expected.

2) *Highly Corrupted GNSS Observations*: Compared to the temporary loss of GNSS observations, we emphasize that including highly corrupted GNSS observations in the graph has a greater impact on estimation performance. This conclusion can be supported by Seq. C02, where the accuracy of our proposed fusion paradigms is significantly degraded in GNSS-corrupted areas, as shown in Fig. 1. In Fig. 13, we plot the estimated trajectories in this scenario by transforming the

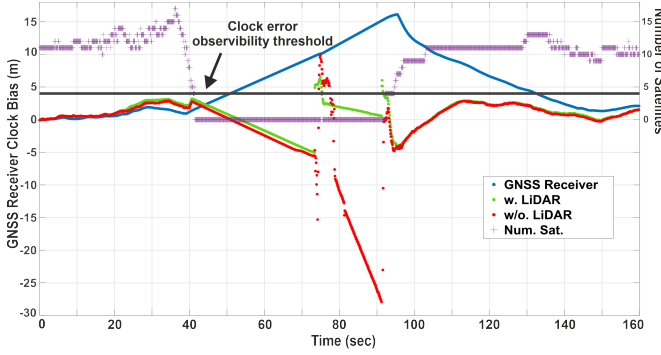


Figure 12: Estimated GNSS receiver clock bias of Seq. C01 without near-zero-velocity detection. The receiver clock error is unobservable during tunnel crossing. In this scenario, fusing raw GNSS observations without lidar odometry cannot constrain the state estimation, resulting in trajectory drifting.

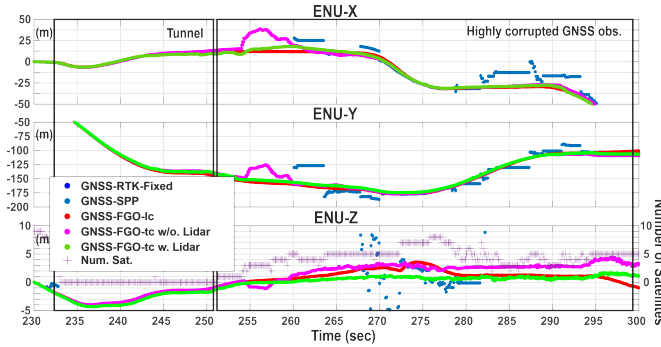


Figure 13: Coordinates in the ENU frame of Seq. C02. The estimated trajectories become unsmooth if the GNSS observations are strongly corrupted in urban areas.

coordinates in the navigation frame (ENU). A large trajectory drift up to 25 m can be observed in tightly coupled fusion without lidar odometry (see Fig. 13). Although fusing relative motion constraints, such as odometry, can effectively constrain divergence, trajectory drifts cannot be eliminated until valid global references are acquired.

3) *Lidar Odometry Degradation*: As discussed in [67], traditional lidar odometry algorithms suffer from dramatic degradation in unstructured environments and high-speed scenarios. This problem can also be observed in our experiments. Fig. 14 illustrates three scenarios in which the accuracy of the lidar odometry is penalized if the vehicle is driving in featureless areas or in high-speed mode with an average vehicle speed of 125 km/h. In low-speed driving mode and open-sky areas, lidar degradation does not reduce the estimation performance while high-quality GNSS measurements are available. However, if the vehicle is moving at high speed, the lidar odometry becomes inaccurate because of motion distortion. Therefore, including lidar odometry factors in the graph can decrease localization accuracy, as presented in Table II of Seq. HS. In scenarios with long tunnels, trajectory drifting can always be expected due to loss of global reference. This presents the major limitation of classic lidar odometers that calculate only pose increments. To overcome this limitation, more observed

state variables, such as vehicle velocity, can be considered [67].

D. Smoother Type and Computation Time

To study the impact of different smoother types and lag sizes, we evaluated batch and incremental smoother *iSAM2* with different lag sizes for Seq. DUS. The performance metrics are presented in Table III. Compared to an incremental smoother, solving the optimization problem with a batch optimizer does not show a considerable improvement in accuracy. This happens because the graph structure becomes more similar to a Markov chain in large-scale localization applications where fewer loop-closure constraints are available. In this scenario, re-linearizing all past state variables does not contribute more information that improves the accuracy. For loosely coupled fusion, the batch smoother presents a smoother trajectory. However, this advantage is absent with the incremental smoother when fusing GNSS observations in a tight coupling.

Furthermore, the batch optimizer requires more computational resources than the incremental smoother (see Fig. 15), especially in urban areas with more measurement outliers. In online applications, estimation accuracy and trajectory smoothness can be penalized once optimization takes longer. This conclusion is supported by referring to the tightly coupled fusion in Table III. Similarly to the optimizer type, considering a large lag size does not contribute significantly. Moreover, even the incremental smoother with a large lag size frequently violates the desired optimization frequency, resulting in inefficient optimization procedures.

Table III: Estimation Performance of Seq. DUS using Different Solver Settings.

Conf.	Mean 2D Pos. Err. (m)	Mean 3D Pos. Err. (m)	Mean Yaw Err. (°)	s
1c-batch-3s	0.324	0.839	0.208	1526.4
1c-isam2-3s	0.397	1.146	0.216	5672.8
tc-batch-3s	1.543	2.008	0.497	1649.3
tc-isam2-10s	1.419	1.733	0.573	1537.9
tc-isam2-3s	1.524	1.766	0.511	1510.5

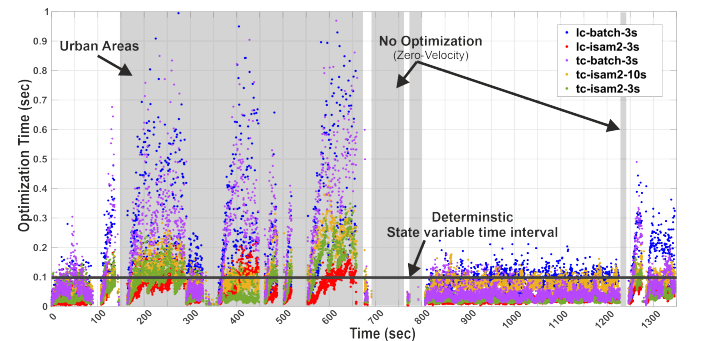


Figure 15: Computation time with different configurations of Seq. DUS.

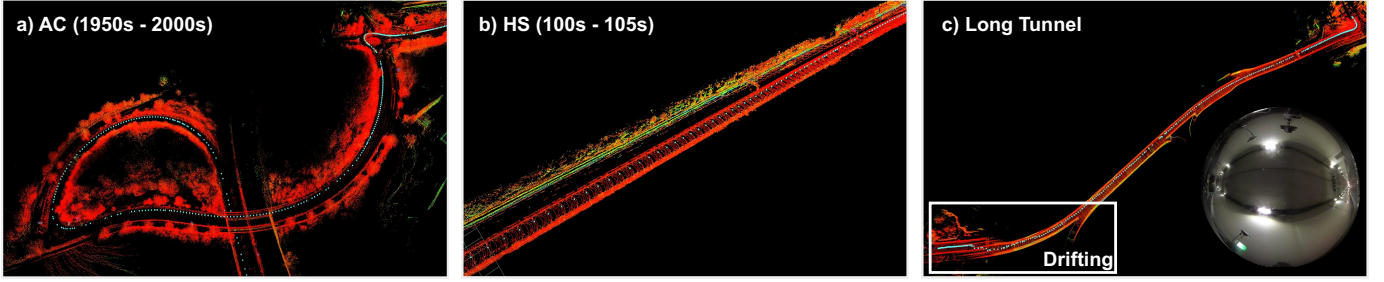


Figure 14: Examples of lidar odometry degradation in three scenarios: a) unstructured feature-less area, b) high-speed scenario and c) long tunnel (400 m).

E. GP-WNOA/WNOJ Motion Model

In this section, we evaluated the continuous-time trajectory representation using the Gaussian process interpolation with both white-noise-on-jerk (GP-WNOJ) and white-noise-on-acceleration (GP-WNOA) models. As introduced in Sec. IV-D, we do not discuss hyper-parameter tuning in this work. The hyper-parameter q_c was manually tuned by penalizing the vehicle pose in Q_c equally for both models.

Compared to the GP-WNOJ model, a GP-WNOA model assumes that the system transition follows a constant velocity model [7, 44]. As discussed in [12], representing vehicle trajectories with an approximately constant-velocity model may be insufficient in urban driving scenarios where the vehicle accelerates and brakes frequently. To evaluate the performance of both GP models, we chose a part of Seq. AC containing 200s test run in open-sky areas where the GNSS-PVA solution presents the ground-truth trajectory. We calculate the whitened error of the vehicle pose and the linear velocity in the body frame and plot the results on the histogram in Fig. 16. Because the GP-WNOJ model represents second-order system dynamics, it shows smaller errors in all linear velocity components. Both models perform similarly in position estimation, where the GP-WNOJ is more accurate in the main motion direction x -axis. For the rotation, the GP-WNOJ does not present considerable improvements compared to the GP-WNOA. One possible reason supporting this result can be traced back to the rotational acceleration that cannot be observed directly using the IMU, as introduced in Sec. V-A.

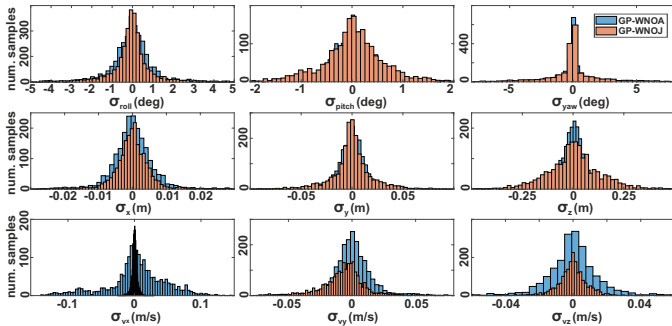


Figure 16: Histogram of whitened state errors of GP models in an open-sky area.

We have validated that the GP motion model formulates a valid continuous-time trajectory representation. However,

tuning the power spectral matrix Q_c that scales the system transition in the Gaussian process kernel has a large effect on numerical stability and estimation performance [12]. Although the GP-WNOJ model presents reliable velocity estimates compared to the GP-WNOA model, it requires more careful parameter tuning when incorporating accelerations in state propagation. For trajectory estimation applications that conduct multi-sensor fusion, the state variables are generally sufficiently constrained by heterogeneous sensor factors, making the data-driven hyper-parameter tuning possible [53].

VIII. CONCLUSION

This article proposes an online factor graph optimization that generalizes multi-sensor fusion for robust trajectory estimation with a focus on GNSS. The vehicle trajectory is represented in continuous time using a Gaussian process motion prior that enables arbitrary state querying, presenting a sensor-independent graph optimization. We successfully fused asynchronous sensor measurements, including GNSS, IMU, vehicle speed sensor, and lidar odometry, into the proposed method for robust vehicle localization in challenging environments. The experimental studies show that the proposed method is robust, flexible, accurate, and works online with multiple datasets collected from different challenging scenarios, including urban areas and high-speed tracks. All our FGO configurations, loosely and tightly coupled with and without lidar, succeed in all test sequences, whereas the classic state-of-the-art lidar-centric method [2] failed in some situations due to scan registration failures. Observed from the experimental results, the GP-WNOJ motion prior enables accurate trajectory representations in continuous time with properly tuned hyper-parameters. In addition, fusing GNSS observations in a tight coupling has demonstrated improved trajectory smoothness and estimation robustness. Future work will include extending GNSS observations with carrier-phases, online parameter tuning, and sensor noise identification.

ACKNOWLEDGMENTS

The authors thank Robin Taborsky from the Institute of Automatic Control at the RWTH Aachen University and the public order office in Aachen, Düsseldorf, and Cologne for their great support in measurement campaigns. We also thank David Yoon and Keenan Burnett from the Autonomous Space Robotics Laboratory at the University of Toronto for their discussions and support in this work.

REFERENCES

- [1] N. Zhu, J. Marais, D. Bétaille, and M. Berbineau, "GNSS position integrity in urban environments: A review of literature," *IEEE Trans. on Intelligent Transportation Systems*, vol. 19, no. 9, pp. 2762–2778, 2018.
- [2] T. Shan, B. Englot, D. Meyers, W. Wang, C. Ratti, and D. Rus, "LIO-SAM: Tightly-coupled LiDAR inertial odometry via smoothing and mapping," *2020 IEEE/RSJ Int. Conf. on Intelligent Robots and Systems (IROS)*, pp. 5135–5142, 2020.
- [3] W. Burgard, O. Brock, and C. Stachniss, *Map-Based Precision Vehicle Localization in Urban Environments*, 2008, pp. 121–128.
- [4] G. Bresson, Z. Alsayed, L. Yu, and S. Glaser, "Simultaneous localization and mapping: A survey of current trends in autonomous driving," *IEEE Trans on Intelligent Vehicles*, vol. 2, no. 3, pp. 194–220, 2017.
- [5] C. Sung, S. Jeon, H. Lim, and H. Myung, "What if there was no revisit? Large-scale graph-based SLAM with traffic sign detection in an HD map using LiDAR inertial odometry," *Intelligent Service Robotics*, vol. 15, pp. 161–170, 2022.
- [6] W. Wen, T. Pfeifer, X. Bai, and L.-T. Hsu, "Factor graph optimization for GNSS/INS integration: A comparison with the extended Kalman filter," *NAVIGATION*, vol. 68, no. 2, pp. 315–331, 2021.
- [7] H. Zhang, X. Xia, M. Nitsch, and D. Abel, "Continuous-Time factor graph optimization for trajectory smoothness of GNSS/INS navigation in temporarily gnss-denied environments," *IEEE Robotics and Automation Letters*, vol. 7, no. 4, pp. 9115–9122, 2022.
- [8] F. Dellaert, "Factor Graphs: Exploiting structure in robotics," *Annual Review of Control, Robotics, and Autonomous Systems*, vol. 4, no. 1, pp. 141–166, 2021.
- [9] L.-T. Hsu, "Analysis and modeling GPS NLOS effect in highly urbanized area," *GPS Solutions*, vol. 22, 11 2017.
- [10] K. Burnett, Y. Wu, D. J. Yoon, A. P. Schoellig, and T. D. Barfoot, "Are we ready for radar to replace lidar in all-weather mapping and localization?" *IEEE Robotics and Automation Letters*, vol. 7, no. 4, pp. 10 328–10 335, 2022.
- [11] J. Jeong, Y. Cho, Y.-S. Shin, H. Roh, and A. Kim, "Complex urban dataset with multi-level sensors from highly diverse urban environments," *The Int. Journal of Robotics Research*, vol. 38, no. 6, pp. 642–657, 2019.
- [12] T. Y. Tang, D. J. Yoon, and T. D. Barfoot, "A White-Noise-on-Jerk motion prior for continuous-time trajectory estimation on SE(3)," *IEEE Robotics and Automation Letters*, vol. 4, no. 2, pp. 594–601, 2019.
- [13] J. Zhang and S. Singh, "Low-drift and real-time LiDAR odometry and mapping," *Autonomous Robots*, vol. 41, pp. 401–416, 02 2017.
- [14] A. Geiger, P. Lenz, and R. Urtasun, "Are we ready for autonomous driving? the kitti vision benchmark suite," in *Conference on Computer Vision and Pattern Recognition (CVPR)*, 2012.
- [15] N. Sünderhauf and P. Protzel, "Towards robust graphical models for gnss-based localization in urban environments," in *Int. Multi-Conference on Systems, Signals & Devices*, 2012, pp. 1–6.
- [16] R. Watson and J. Gross, "Robust navigation in GNSS degraded environment using graph optimization," in *30th Int. Technical Meeting of the Satellite Division of The Institute of Navigation*, 09 2017.
- [17] P. Groves, *Principles of GNSS, Inertial, and Multisensor Integrated Navigation Systems, Second Edition*. Artech House, 2013.
- [18] W. Wen, Y. C. Kan, and L.-T. Hsu, "Performance comparison of GNSS/INS integrations based on EKF and factor graph optimization," in *Proc. of 32th Int. Technical Meeting of the Satellite Division of The Institute of Navigation*, 09 2019, pp. 3019–3032.
- [19] W. Wen, X. Bai, Y. C. Kan, and L.-T. Hsu, "Tightly coupled GNSS/INS integration via factor graph and aided by fish-eye camera," *IEEE Trans. on Vehicular Technology*, vol. 68, no. 11, pp. 10 651–10 662, 2019.
- [20] W. Wen and L.-T. Hsu, "Towards robust GNSS positioning and real-time kinematic using factor graph optimization," in *2021 IEEE Int. Conf. on Robotics and Automation (ICRA)*, 2021, pp. 5884–5890.
- [21] X. Bai, W. Wen, and L.-T. Hsu, "Time-correlated window-carrier-phase-aided GNSS positioning using factor graph optimization for urban positioning," *IEEE Trans. on Aerospace and Electronic Systems*, vol. 58, no. 4, pp. 3370–3384, 2022.
- [22] T. Suzuki, "GNSS Odometry: Precise trajectory estimation based on carrier phase cycle slip estimation," *IEEE Robotics and Automation Letters*, vol. 7, no. 3, pp. 7319–7326, 2022.
- [23] B. Congram and T. D. Barfoot, "Field testing and evaluation of single-receiver gps odometry for use in robotic navigation," *Field Robotics*, vol. 2, pp. 1849–1873, 2022.
- [24] T. Pfeifer, P. Weissig, S. Lange, and P. Protzel, "Robust factor graph optimization - a comparison for sensor fusion applications," in *2016 IEEE 21st Int. Conf. on Emerging Technologies and Factory Automation (ETFA)*, 2016, pp. 1–4.
- [25] R.M. Watson and J. N. Gross, "Robust Navigation In GNSS Degraded Environment Using Graph Optimization," 30th Int. Tech. Meeting of the Satellite Division of The Institute of Navigation, Sep 2017, pp. 2906–2918.
- [26] T. Suzuki, "1st place winner of the smartphone decimeter challenge: Two-step optimization of velocity and position using smartphone's carrier phase observations," in *Proc. of the 35th Int. Technical Meeting of the Satellite Division of The Institute of Navigation*, 09 2022, pp. 2276–2286.
- [27] T. Pfeifer and P. Protzel, "Incrementally learned mixture models for GNSS localization," in *2019 IEEE Intelligent Vehicles Symposium (IV)*, 2019, pp. 1131–1138.
- [28] W. Wen, G. Zhang, and L.-T. Hsu, "GNSS outlier mitigation via graduated non-convexity factor graph optimization," *IEEE Trans. on Vehicular Technology*, vol. 71, no. 1, pp. 297–310, 2022.
- [29] K. Koide, J. Miura, and E. Menegatti, "A portable three-dimensional lidar-based system for long-term and wide-area people behavior measurement," *Int. Journal of Advanced Robotic Systems*, vol. 16, no. 2, p. 1729881419841532, 2019.
- [30] J. Zhang, W. Wen, H. Feng, X. Chen, and L.-T. Hsu, "Continuous GNSS-RTK aided by LiDAR/Inertial odometry with intelligent GNSS selection in urban canyons," in *Proc. of 34th Int. Technical Meeting of the Satellite Division of The Institute of Navigation*, 09 2021, pp. 4198–4207.
- [31] Z. Gong, P. Liu, F. Wen, R. Ying, X. Ji, R. Miao, and W. Xue, "Graph-based adaptive fusion of GNSS and VIO under intermittent GNSS-degraded environment," *IEEE Trans. on Instrumentation and Measurement*, vol. 70, pp. 1–16, 2021.
- [32] S. Cao, X. Lu, and S. Shen, "GVINS: tightly coupled GNSS–Visual–Inertial fusion for smooth and consistent state estimation," *IEEE Trans. on Robotics*, vol. 38, no. 4, pp. 2004–2021, 2022.
- [33] W. Wen, X. Bai, and L.-T. Hsu, "3D vision aided GNSS real-time kinematic positioning for autonomous systems in urban canyons," *NAVIGATION: Journal of the Institute of Navigation*, vol. 70, no. 3, 2023.
- [34] Y. Wang, W. Song, Y. Lou, Y. Zhang, F. Huang, Z. Tu, and Q. Liang, "Rail vehicle localization and mapping with LiDAR-vision-inertial-GNSS fusion," *IEEE Robotics and Automation Letters*, vol. 7, no. 4, pp. 9818–9825, 2022.
- [35] D. Wisth, M. Camurri, S. Das, and M. Fallon, "Unified multi-modal landmark tracking for tightly coupled LiDAR-Visual-Inertial odometry," *IEEE Robotics and Automation Letters*, vol. 6, no. 2, pp. 1004–1011, 2021.
- [36] W. Shao, S. Vijayarangan, C. Li, and G. Kantor, "Stereo Visual Inertial LiDAR simultaneous localization and mapping," in *2019 IEEE/RSJ Int. Conf. on Intelligent Robots and Systems (IROS)*, 2019, pp. 370–377.
- [37] J. Nubert, S. Khattak, and M. Hutter, "Graph-based multi-sensor fusion for consistent localization of autonomous construction robots," in *2022 Int. Conf. on Robotics and Automation (ICRA)*, 2022, pp. 10 048–10 054.
- [38] S. Zhao, H. Zhang, P. Wang, L. Nogueira, and S. Scherer, "Super Odometry: IMU-centric LiDAR-Visual-Inertial estimator for challenging environments," in *2021 IEEE/RSJ Int. Conf. on Intelligent Robots and Systems (IROS)*, 2021, pp. 8729–8736.
- [39] G. Cioffi and D. Scaramuzza, "Tightly-coupled fusion of global positional measurements in optimization-based visual-inertial odometry," in *2020 IEEE/RSJ Int. Conf. on Intelligent Robots and Systems (IROS)*, 2020, pp. 5089–5095.
- [40] S. Boche, X. Zuo, S. Schaefer, and S. Leutenegger, "Visual-inertial SLAM with tightly-coupled dropout-tolerant GPS fusion," in *2022 IEEE/RSJ Int. Conf. on Intelligent Robots and Systems (IROS)*, 2022, pp. 7020–7027.
- [41] C. Hu, S. Zhu, Y. Liang, and W. Song, "Tightly-coupled visual-inertial-pressure fusion using forward and backward imu preintegration," *IEEE Robotics and Automation Letters*, vol. 7, no. 3, pp. 6790–6797, 2022.
- [42] P. Furgale, T. D. Barfoot, and G. Sibley, "Continuous-time batch estimation using temporal basis functions," in *2012 IEEE Int. Conf. on Robotics and Automation*, 2012, pp. 2088–2095.
- [43] D. Hug, P. Bänninger, I. Alzugaray, and M. Chli, "Continuous-time stereo-inertial odometry," *IEEE Robotics and Automation Letters*, vol. 7, no. 3, pp. 6455–6462, 2022.
- [44] T. D. Barfoot, C. H. Tong, and S. Särkkä, "Batch continuous-time trajectory estimation as exactly sparse Gaussian process regression," in *Robotics: Science and Systems*, 2014.

- [45] M. Mukadam, J. Dong, F. Dellaert, and B. Boots, "STEAP: simultaneous trajectory estimation and planning," *Autonomous Robots*, vol. 43, 02 2019.
- [46] X. Yan, V. Indelman, and B. Boots, "Incremental sparse GP regression for continuous-time trajectory estimation and mapping," *Robotics and Autonomous Systems*, vol. 87, pp. 120–132, 2017.
- [47] J. Dong, J. G. Burnham, B. Boots, G. C. Rains, and F. Dellaert, "4D Crop Monitoring: Spatio-temporal reconstruction for agriculture," *2017 IEEE Int. Conf. on Robotics and Automation (ICRA)*, pp. 3878–3885, 2017.
- [48] M. Warren, M. Greeff, B. Patel, J. Collier, A. P. Schoellig, and T. D. Barfoot, "There's no place like home: Visual teach and repeat for emergency return of multirotor uavs during gps failure," *IEEE Robotics and Automation Letters*, vol. 4, no. 1, pp. 161–168, 2019.
- [49] F. Dellaert and M. Kaess, "Factor graphs for robot perception," *Foundations and Trends® in Robotics*, vol. 6, no. 1-2, pp. 1–139, 2017.
- [50] J. Subirana, J. Zornoza, M. Hernández-Pajares, E. S. Agency, and K. Fletcher, *GNSS Data Processing*, ser. ESA TM. ESA Communications, 2013, no. Bd. 1. [Online]. Available: <https://books.google.de/books?id=RO8xngEACAAJ>
- [51] T. D. Barfoot, *State Estimation for Robotics*, 1st ed. USA: Cambridge University Press, 2017.
- [52] S. Anderson and T. D. Barfoot, "Full STEAM ahead: Exactly sparse Gaussian process regression for batch continuous-time trajectory estimation on SE(3)," in *2015 IEEE/RSJ Int. Conf. on Intelligent Robots and Systems (IROS)*, 2015, pp. 157–164.
- [53] J. N. Wong, D. J. Yoon, A. P. Schoellig, and T. D. Barfoot, "A data-driven motion prior for continuous-time trajectory estimation on SE(3)," *IEEE Robotics and Automation Letters*, vol. 5, no. 2, pp. 1429–1436, 2020.
- [54] T. D. Barfoot and P. T. Furgale, "Associating uncertainty with three-dimensional poses for use in estimation problems," *IEEE Trans. on Robotics*, vol. 30, no. 3, pp. 679–693, 2014.
- [55] J. Dong, M. Mukadam, B. Boots, and F. Dellaert, "Sparse Gaussian processes on matrix lie groups: A unified framework for optimizing continuous-time trajectories," in *2018 IEEE Int. Conf. on Robotics and Automation (ICRA)*, 2018, pp. 6497–6504.
- [56] J.-J. Gehrt, M. Nitsch, D. Abel, and R. Zweigel, "High accuracy navigation filter with dual antenna enabling double-differencing with dual-constellation," in *32nd Int. Technical Meeting of the Satellite Division of the Institute of Navigation*, 10 2019, pp. 2186–2197.
- [57] T. Shan and B. Englot, "LeGO-LOAM: Lightweight and ground-optimized LiDAR odometry and mapping on variable terrain," in *2018 IEEE/RSJ Int. Conf. on Intelligent Robots and Systems (IROS)*, 2018, pp. 4758–4765.
- [58] T. Lupton and S. Sukkariyeh, "Visual-Inertial-aided navigation for high-dynamic motion in built environments without initial conditions," *IEEE Trans. on Robotics*, vol. 28, no. 1, pp. 61–76, 2012.
- [59] C. Forster, L. Carlone, F. Dellaert, and D. Scaramuzza, "On-manifold preintegration for real-time visual-inertial odometry," *IEEE Trans. on Robotics*, vol. PP, 08 2016.
- [60] M. Agrawal, "A lie algebraic approach for consistent pose registration for general euclidean motion," in *2006 IEEE/RSJ Int. Conf. on Intelligent Robots and Systems*, 2006, pp. 1891–1897.
- [61] J. T. Barron, "A general and adaptive robust loss function," in *2019 IEEE/CVF Conference on Computer Vision and Pattern Recognition (CVPR)*, 2019, pp. 4326–4334.
- [62] K. MacTavish and T. D. Barfoot, "At all costs: A comparison of robust cost functions for camera correspondence outliers," in *2015 12th Conference on Computer and Robot Vision*, 2015, pp. 62–69.
- [63] S. W. Anderson, "Batch continuous-time trajectory estimation," PhD thesis, University of Toronto, 4925 Dufferin Street, Toronto, ON M3H 5T6 CA, June 2017, available at <https://hdl.handle.net/1807/77974>.
- [64] A. Ranganathan, M. Kaess, and F. Dellaert, "Fast 3D pose estimation with out-of-sequence measurements," in *2007 IEEE/RSJ Int. Conf. on Intelligent Robots and Systems (IROS)*, 2007, pp. 2486–2493.
- [65] M. Kaess, H. Johannsson, R. Roberts, V. Ila, J. Leonard, and F. Dellaert, "iSAM2: Incremental smoothing and mapping with fluid relinearization and incremental variable reordering," in *2011 IEEE Int. Conf. on Robotics and Automation*, 2011, pp. 3281–3288.
- [66] D. Wisth, M. Camurri, and M. Fallon, "Vilens: Visual, inertial, lidar, and leg odometry for all-terrain legged robots," *IEEE Trans. on Robotics*, vol. 39, no. 1, pp. 309–326, 2023.
- [67] D. J. Yoon, K. Burnett, J. Laconte, Y. Chen, H. Vhavle, S. Kammel, J. Reuther, and T. D. Barfoot, "Need for speed: Fast correspondence-free lidar odometry using doppler velocity," in *2023 IEEE/RSJ Int. Conf. on Intelligent Robots and Systems (IROS)*, 2023.